

1 Diversity-driven, efficient exploration of a MOF design space to optimize MOF properties

2 Tsung-Wei Liu,^{†,a} Quan Nguyen^{†,b}, Adji Bouso Dieng^{c*}, Diego A. Gómez-Gualdrón^{a*}

3 ^a Department of Chemical and Biological Engineering, Colorado School of Mines, 1601 Illinois St, Golden CO 80401, USA

4 ^b Department of Computer Science and Engineering, Washington University in St. Louis, 1 Brookings Dr, St. Louis MO 63130, USA

5 ^c Vertaix, Department of Computer Science, Princeton University, 35 Olden St, Princeton NJ 08540, USA

6 [†] These authors contributed equally

7 * Corresponding authors: dgomezgualdron@mines.edu

8 adji@princeton.edu

9 ABSTRACT

10 Metal-organic frameworks (MOFs) promise to engender technology-enabling properties for numerous applications. However, one
11 significant challenge in MOF development is their overwhelmingly large design space, which is intractable to fully explore even
12 computationally. To find diverse optimal MOF designs without exploring the full design space, we develop Vendi Bayesian optimization
13 (VBO), a new algorithm that combines traditional Bayesian optimization with the Vendi Score, a recently introduced interpretable
14 diversity measure. Both Bayesian optimization and the Vendi Score require a kernel similarity function, we therefore also introduce a
15 novel similarity function in the space of MOFs that accounts for both chemical and structural features. This new similarity metric enables
16 VBO to find optimal MOFs with properties that may depend on both chemistry and structure. We statistically assessed VBO by its
17 ability to optimize three NH₃-adsorption dependent performance metrics that depend, to different degrees, on MOF chemistry and
18 structure. With ten simulated campaigns done for each metric, VBO consistently outperformed random search to find high-performing
19 designs within a 1,000-MOF subset for *i*) NH₃ storage, *ii*) NH₃ removal from membrane plasma reactors, and *iii*) NH₃ capture from air.
20 Then, with one campaign dedicated to finding optimal MOFs for NH₃ storage in a “hybrid” ~10,000-MOF database, we identify twelve
21 extant and eight hypothesized MOF designs with potentially record-breaking working capacity ΔN_{NH_3} between 300 K and 400 K at 1
22 bar. Specifically, the best MOF designs are predicted to *i*) achieve ΔN_{NH_3} values between 23.6 and 29.3 mmol/gm, potentially surpassing
23 those that MOFs previously experimentally tested for NH₃ adsorption would have at the proposed operation conditions, *ii*) be thermally
24 stable at the operation conditions and *iii*) require only ca. 10% of the energy content in NH₃ to release the stored molecule from the
25 MOF. Finally, the analysis of the generated simulation data during the search indicates that a pore size of around 10 Å, a heat of
26 adsorption around 33 kJ/mol, and the presence of Ca could be part of MOF design rules that could help optimize NH₃ working capacity
27 at the proposed operation conditions.

28 **KEYWORDS:** Bayesian Optimization, Active Learning, Vendi Score, Machine Learning, Materials Screening, Ammonia Storage

29

30 1. INTRODUCTION

31 Metal-organic frameworks (MOFs) are a class of porous
32 materials that could be bestowed with properties that could
33 enable technological breakthroughs in energy, environment,
34 and other fields.¹⁻⁴ The idea is that judicious selection of MOF
35 constituent nodes and linkers could yield whichever
36 architecture and/or chemistry is required to engender the
37 necessary material property or behavior to enable the
38 breakthrough.⁵ However, one persisting challenge in MOF
39 development has been that the combinatorics of constituent
40 building blocks creates an overwhelmingly large material
41 “design space.”^{6,7,8} To expedite the navigation of the MOF
42 design space, for longer than a decade, MOF development has
43 been aided by high throughput computation instead of solely
44 relying on experiments.⁹⁻¹¹

45 High throughput computation in MOFs has usually
46 relied on exhaustively predicting key performance-relevant
47 properties in all MOFs in a database—usually using molecular
48 simulation.^{12,13} Some notable databases have been created out
49 of experimentally reported MOF structures (i.e. extant MOFs)¹⁴
50 curated from the Cambridge Structure Database, or

51 hypothesized MOF structures outputted by crystal creation
52 codes (i.e. MOF prototypes).^{6,15-17} Notable databases of extant
53 MOFs have been created by Chung *et al.*¹⁴ (~20k MOFs) and
54 by Moghadam *et al.*¹⁸ (~70k MOFs). On the other hand, notable
55 databases of hypothesized MOFs include those created by
56 Wilmer *et al.*¹⁵ (~137k MOFs), Colon *et al.*¹⁹ (~13k MOFs),
57 Boyd *et al.*²⁰ (~280k MOFs), among others. Note, however, that
58 the size of these databases is very small compared to the
59 vastness of the MOF design space, which some estimate to span
60 at least one trillion MOFs.²¹

61 Indeed, current computational capabilities only allows
62 evaluating a small number of MOFs relative to the MOF design
63 space size. For instance, the work by Simon *et al.*¹³ only
64 managed to predict methane adsorption in ~650k materials,
65 even though methane adsorption is one of the fastest properties
66 to predict by simulation.²² Calculation of other properties have
67 proven even more limiting. For instance, prediction of charge
68 distribution through density functional theory (DFT) by
69 Nazarian *et al.*²³ was limited to ~3k structures. Prediction of
70 band gaps via DFT by Rosen *et al.*²⁴ was limited to ~20k
71 structures. Prediction of thermal conductivity by Islamov *et al.*⁹
72 via molecular dynamics was limited to ~10k structures.

1 Predictions of hexane isomer mixture adsorption by Chung *et al.*²⁵ was limited to ~500 structures. Moreover, in the case of
2 adsorption applications, computational limits may be even
3 more restrictive since screening for such properties for a given
4 application may require considering different conditions in
5 temperature, pressure, and composition (in the case of
6 mixtures).

7 One can argue that the discovery of technology-
8 enabling MOFs have been hampered by the inability to explore
9 the MOF design space at large. One way that researchers have
10 attempted to expand the number of MOFs considered in a given
11 study is through hierarchical screening. But the latter first
12 requires the calculation of an inexpensive descriptor which
13 (hopefully) points to (smaller) regions of the MOF design space
14 where the property of interest may have desirable values.²⁵⁻²⁷
15 Therefore, hierarchical screening presents caveats such as: *i*)
16 requiring extensive “domain knowledge” to identify an
17 effective, inexpensive “descriptor”²⁸ *ii*) still being unlikely that
18 the descriptor can be calculated on the MOF design space at
19 large, *iii*) due to a probably imperfect correlation, still being
20 possible that the descriptor calculation may overlook regions of
21 design space where the property of interest could have desirable
22 values.

23 Hence, there is growing interest in methods that allow
24 exploring the MOF design space efficiently, while still relying
25 solely on direct property calculations. For instance, genetic
26 algorithms (GAs) have been explored to evolve an initial small
27 subset of MOFs into new subsets of MOFs with optimized
28 values of the property of interest (e.g., pre-combustion CO₂
29 capture properties,²⁹ or CH₄ storage properties²¹). However, it
30 is understood that GAs tend to require a larger number of
31 evaluations and are slower than other sophisticated
32 search/optimization methods. GAs thus may become rapidly
33 intractable as property calculation becomes more
34 computationally expensive. In contrast, Bayesian optimization
35 is known to be a more sample-efficient method,³⁰ and hence is
36 finding success in tasks such as screening molecules with high
37 power conversion efficiency for clean energy,³¹ optimizing
38 reactions for molecular synthesis³², and finding low-energy
39 molecular conformers,³³ among others.³⁴⁻³⁶

40 The potential benefits of Bayesian methods to
41 optimize porous materials have been suggested by work by
42 Simon and coworkers.³⁷ Working with the data from previously
43 screened ~70k covalent-organic frameworks (COFs), these
44 authors showed that Bayesian optimization could find ca. 50%
45 of the top-100 adsorbents for methane storage only exploring
46 ca. 1% of the COFs. However, the approach used by these
47 authors may not generalize well to searches aiming to optimize
48 other material properties. For instance, their representation of
49 the adsorbent consisted of a 12-component vector of five
50 common (global) textural properties and simple counts of seven
51 specific chemical elements. Such simple representation likely
52 leverages that methane adsorption is primarily a (relatively)
53 smooth function of textural properties. However, it may not be
54 suitable when the property of interest also depends strongly on
55 material chemistry.

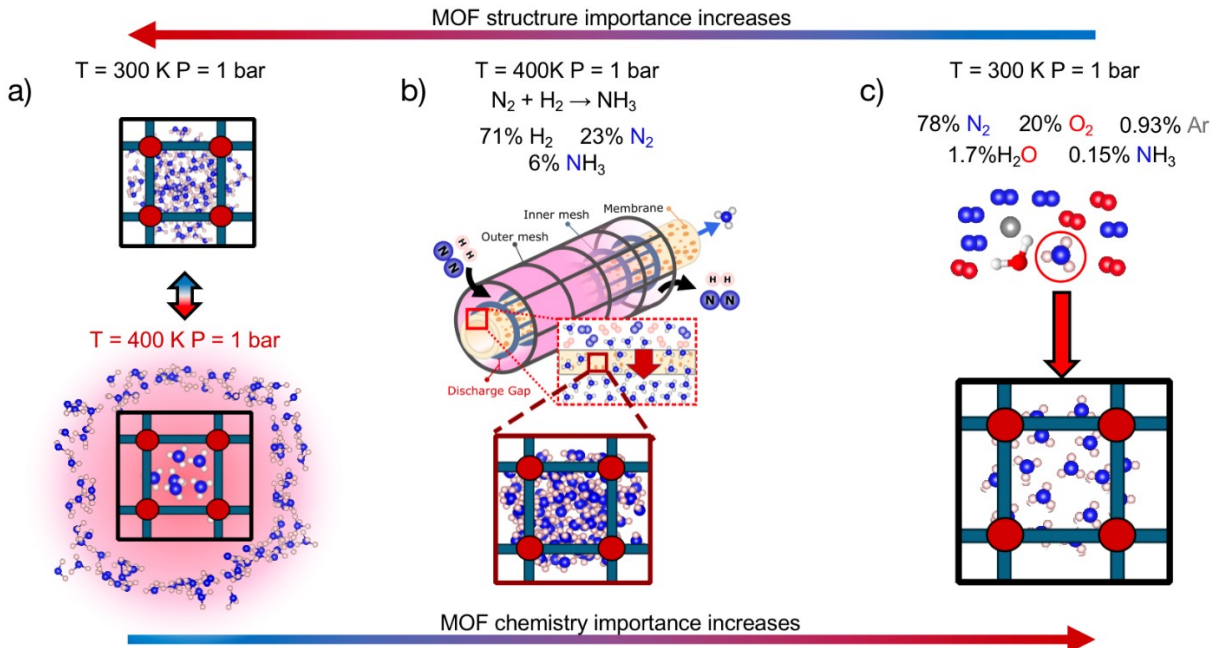
56 On the other hand, traditional Bayesian optimization
57 is designed to find one single optimal solution, which may turn
58 out to correspond to a MOF design that may not be

59 experimentally synthesizable or stable, or for which the
60 performance prediction may have turned out to be unreliable.
61 The task of optimizing a MOF performance metric while
62 ensuring other properties (e.g., synthesizability and stability)
63 also have desirable values can be framed as a multi-objective
64 optimization problem. Such formulation, however, assumes
65 that all relevant metrics are known *a priori* and can be evaluated
66 in similar manners.^{26,38} Multi-objective optimization cannot be
67 realized, however, if some objectives can only be evaluated
68 after screening is completed, or if we cannot anticipate all
69 possible factors that should be accounted for during the search
70 (i.e., prediction reliability for each particular MOF). We thus
71 take a different approach: finding multiple MOFs, different
72 from one another, with desirable predicted values for the
73 primary property of interest.

74 Specifically, in this work, we build a general and
75 efficient framework for searching and finding several optimal
76 MOF designs that are distinct from each other. Our framework
77 is designed to be amenable to performance metrics that depend
78 strongly on either MOF chemistry or textural properties, or both.
79 More specifically, we combine the traditional tools of Bayesian
80 optimization with the Vendi Score—a statistical measure of
81 diversity developed by Friedman and Dieng³⁹—to find a
82 diverse set of promising MOF designs, each yielding a
83 sufficiently high value for the metric of interest, instead of
84 committing to a single optimal MOF that may not be
85 synthesizable or stable. This comes in the form of promoting
86 more exploration in the behavior of our optimization algorithm,
87 selecting MOFs that are diverse from those already inspected.
88 We name this framework Vendi Bayesian optimization (VBO).

89 We first statistically test the efficacy of combining a
90 chemistry- and structure-aware MOF representation with VBO,
91 using a randomly drawn subset of ~1,000 MOFs as a testbed.
92 We conducted these tests on the optimization of three
93 performance metrics depending on the adsorption of NH₃. We
94 chose metrics involving this molecule because NH₃ is important
95 for our society as a precursor to fertilizers,⁴⁰ and could gain
96 further prominence in the near future as an energy vector.⁴¹
97 From an application perspective, the three chosen metrics are
98 relevant to rank MOFs for their potential to help make the
99 synthesis of NH₃ sustainable and carbon-free,⁴² and NH₃
100 storage and transportation easy, energy-efficient and safe.⁴³⁻⁴⁵
101 From a methods perspective, the three chosen metrics pose
102 different challenges to our developed search method. Namely,
103 the polarity of ammonia⁴⁶ and the different adsorption
104 conditions associated with each application (Fig. 1) make the
105 different metrics to balance differently their dependence on
106 MOF chemistry and textural properties (*vide infra*). On the
107 other hand, each metric present different (mathematical)
108 complexity on their relation to adsorption loadings.

109 Upon statistical testing of VBO efficacy, we finish this
110 work with a real search campaign on a ~10,000-MOF hybrid
111 database (i.e., containing extant and hypothesized structures) to
112 find MOFs with outstanding predicted NH₃ storage
113 performance. We chose this application for the real search due
114 to the growing interest of experimentalist chemists in the use of
115 MOFs for NH₃ storage as reflected by the growing number of
116 NH₃ adsorption measurements at 1 bar and 300 K (i.e., ambient
117 conditions) reported in recent years. For instance, Moribe *et al.*
118



3 **Figure 1.** Applications for which NH₃ adsorption-based MOF performance metrics were optimized to test the efficacy of our Vendi Bayesian
4 optimization (VBO) framework. a) Adsorptive NH₃ storage at ambient conditions with release at 400 K and 1 bar. b) Membrane-based NH₃ removal from plasma
5 reactors during NH₃ synthesis at 400 K and 1 bar. c) Dilute NH₃ capture from air in adsorbent traps at ambient conditions. Gas-phase composition
6 relevant to each application indicated at the top. The three chosen metrics present different levels of dependence on MOF chemistry and structure.

7 reported 10.5 mmol_{NH3}/g_{MOF} in Ga-PMOF,⁴⁷ Guo *et al.* 12.8
8 mmol_{NH3}/g_{MOF} in MIL-160,⁴⁸ Kim *et al.* 23.9 mmol_{NH3}/g_{MOF} in
9 Mg-MOF-74⁴⁹ and 23.5 mmol_{NH3}/g_{MOF} in Ni_{acryl}TMA⁵⁰,
10 and Shi *et al.* 33.9 mmol_{NH3}/g_{MOF} in LiCl-MIL-53,⁵¹ among
11 others.^{52,53} But despite growing interest, not much has been
12 done to leverage search algorithms to identify promising MOFs
13 for NH₃ storage. Thus, here we show how our developed VBO,
14 a novel search algorithm for MOFs, can be used to fill such
15 knowledge gaps. Furthermore, our analysis of the MOFs
16 explored by our VBO provides new design rules to guide
17 experimentalists developing MOFs for NH₃ storage.

18 2. SIMULATION METHODS

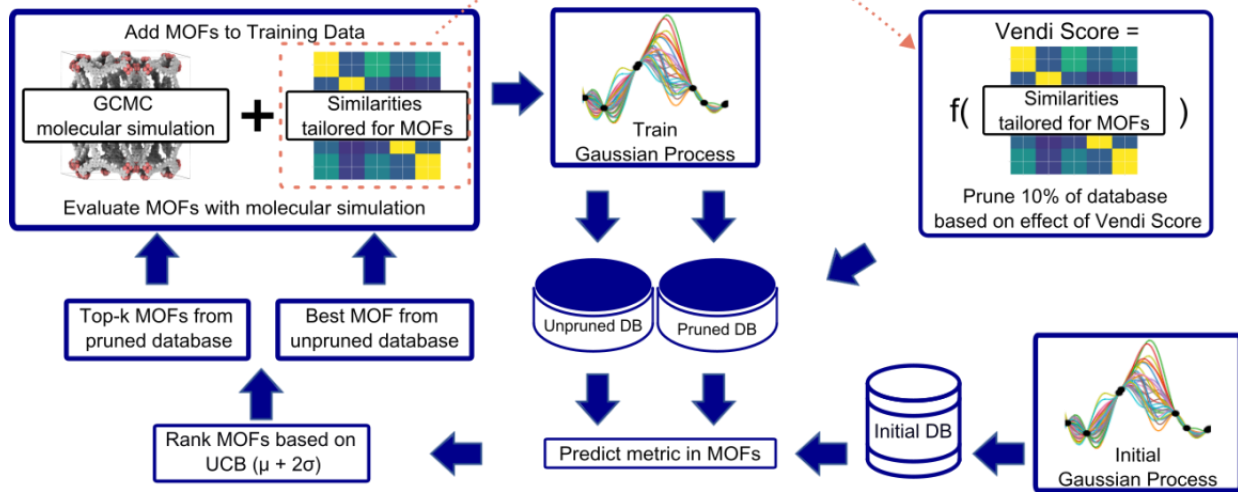
19 **2.1. MOF database** About 12,000 structures from the 2019
20 CoRE MOF database¹⁴ and about 3,000 structures created
21 earlier using ToBaCCo-3.0⁶ were used as a starting point to
22 ultimately create a hybrid database of ~10,000 structures. These
23 MOF sources are complementary. CoRE MOFs are extant
24 structures with high, but non-systematic, chemical and
25 structural diversity that tend to feature small pores.⁵⁴ ToBaCCo
26 MOFs are hypothesized structures with systematic, but medium,
27 chemical and structural diversity that feature medium to large
28 pores.⁵⁴ All MOFs underwent characterization of their void
29 fraction, surface area, and pore size distribution using zeo++. A
30 probe radius of 1.3 Å was used by zeo++ to determine the
31 accessibility of pores through the percolation algorithm.⁵⁵ Then
32 a probe of same size was used to determine the characteristic of
33 the accessible pores. Note that the radius of 1.3 Å is adopted to
34 match the kinetic radius of NH₃.⁵⁶ Failures during
35 characterization calculations and assignment of charges to
36 MOF atoms (see Section 2.2) ultimately reduced the total
37 number of structures available for this work to around 10,000.

38 2.2. Monte Carlo simulations.

39 Monte Carlo simulations were done using RASPA-2.0.^{57,58}
40 Grand canonical Monte Carlo (GCMC) was used to predict
41 adsorption loadings. Temperature and partial pressures of
42 adsorbates in the gas phase were kept constant at the values
43 relevant for the adsorption conditions of interest. Each
44 simulation consisted of 10,000 equilibration cycles, followed
45 by 10,000 production cycles. Each cycle consisted of as many
46 Monte Carlo moves as molecules there are in the simulation box,
47 but never less than 20. Moves corresponded to
48 insertion/deletion, translation, and rotation (and swap for
49 mixture cases). The Widom insertion method,⁵⁹ with at least
50 10,000 insertion moves, was used to calculate Henry's
51 constants at the temperature of interest. Molecular interactions
52 were modeled using the Lennard-Jones (LJ) and Coulomb
53 potential. A cutoff of 12.8 Å was used for the LJ potential, and
54 12.0 Å for the Coulomb potential, after which distance Ewald
55 summation was used.^{60,61} LJ parameters and charges for NH₃
56 and N₂ molecules were assigned according to the Trappe force
57 field^{62,63} for H₂O according to the TIP4P model,⁶⁴⁻⁶⁶ whereas
58 for H₂ were obtained from the work by Levesque *et al.*^{67,68} LJ
59 parameters for MOF atoms were assigned according to the
60 Dreiding force field,⁶⁹ or universal force field⁷⁰ if parameters
61 from Dreiding were unavailable. LJ parameters for cross-
62 interactions were obtained using Lorentz-Berthelot mixing
63 rules. Note that the above LJ parameter selection have been
64 used by Snurr and coworkers, and several others, to model NH₃
65 adsorption in MOFs.⁷¹⁻⁷⁵ Charges for MOF atoms were
66 assigned based on the best method available for each MOF
67 subset. Thus, charges in ToBaCCo MOFs were assigned in

earlier work using the MBBB method,⁷⁶ whereas for atoms in CoRE MOFs, charges were assigned using PACMOF.⁷⁷ MBBB

3



4

Figure 2. Workflow for our VBO framework. An initial GP, trained with data for two randomly chosen MOFs, is used to predict the performance metric in the starting database. $k+1$ MOFs are selected for molecular simulation evaluation based on the upper confidence bound (UCB) acquisition function. One MOF is chosen as the MOF scoring the highest UCB just as in standard Bayes optimization. The remaining k MOFs are selected based on UCB but only after 10% of the database is pruned. The MOFs pruned from the database are the MOFs that would increase the least the Vendi Score of the cumulative set of MOFs evaluated by molecular simulation. The top $k+1$ MOFs selected are then evaluated using molecular simulations. To perform a new iteration, the molecular simulation data for the newly evaluated $k+1$ MOFs are added to the data for training the GP, and the MOF selection process is repeated.

is based on DFT calculations on MOF building blocks, which are directly inherited by the MOF, when constructed by ToBaCCo. PACMOF, on the other hand, is a machine learning model that was trained by Snurr and coworkers, from DFT calculations on complete MOF unit cells, to predict charges in MOF atoms, with an accuracy of $0.02e$ in mean absolute error ($R^2 = 0.99$). Moreover, the higher accuracy of PACMOF over other fast charge assignments was recently shown by Liu and Luan.⁷⁸ Example comparison between simulated adsorption isotherms using the methods herein against experimental ones are shown in Fig. S2.

2.3. Assessed performance metrics.

NH_3 storage. The incumbent method to store NH_3 relies on condensation at temperatures in the 238 to 253 K range, under pressures in the 10 to 15 bar range.^{38,79} Exploration of adsorptive NH_3 storage in the literature coincide on storing NH_3 at ambient conditions (300 K and 1 bar), but do not present consensus on the desired conditions for the release. Importantly, however, the performance of an adsorbent for ammonia storage depends on both the amount of NH_3 trapped at the storage conditions, $N_{\text{NH}_3}^{\text{ads}}$, and that retained in the adsorbent at the release conditions, $N_{\text{NH}_3}^{\text{des}}$. The difference between these two quantities defines the working (effective) storage capacity ΔN_{NH_3} as:

$$\Delta N_{\text{NH}_3} = N_{\text{NH}_3}^{\text{ads}} - N_{\text{NH}_3}^{\text{des}} \quad (1)$$

Due to its technical simplicity, here we consider the release of ammonia to be done simply by heating the adsorbent to 400K at 1 bar (Fig. 1a). Note that as having enough space in the MOF pore is paramount to this application, ΔN_{NH_3} is expected to be strongly influenced by MOF textural features such as pore size, void fraction and so forth.

NH_3 removal during plasma-assisted synthesis. The incumbent method to make NH_3 typically uses a pressure of 150 bar and a temperature of 650 K. However, as it turns out, sustainable, carbon-free NH_3 production requires synthesis at mild conditions.⁸⁰⁻⁸² A promising method for NH_3 synthesis at 1 bar and 400 K is plasma-assisted synthesis in dielectric barrier discharge (DBD) reactors. In these reactors, low synthesis temperature is enabled by the accelerated breakdown of reactant molecules (N_2 and H_2) due to collisions with high-energy electrons in the plasma. But these electrons can also break down some of the freshly formed ammonia. Thus, a plasma reactor configuration that incorporates a porous membrane that remove ammonia as it forms, could protecting NH_3 from plasma decomposition (Fig. 1b), increasing energy efficiency.^{83,84} One of the desirable characteristics for the porous membrane are high adsorption of ammonia N_{NH_3} at the reaction conditions, but with high adsorption selectivity for ammonia α_{NH_3} over N_2 and H_2 , where:

$$\alpha_{\text{NH}_3} = (N_{\text{NH}_3}/y_{\text{NH}_3})/((\sum N_i)/(\sum y_i)) \quad (2)$$

where y_{NH_3} is the molar fraction of NH_3 in the gas phase, and N_i and y_i are the adsorbed loading and molar fractions in the gas phase, respectively, of all other species i . Assuming a 3:1 $\text{H}_2:\text{N}_2$ feed ratio and a conversion of 10 %, here y_{NH_3} , y_{N_2} and y_{H_2} are assumed to be 0.06, 0.23, 0.71, respectively. Seeking to account for both adsorption and selectivity, here we use M_{ATS} as a performance metric where:

$$M_{\text{ATS}} = \alpha_{\text{NH}_3} \times N_{\text{NH}_3} \quad (3)$$

Note that selectivity, α_{NH_3} , is a reflection of the attraction of the MOF to NH_3 relative to N_2 and H_2 , and hence is expected to be strongly influenced by chemistry. On the other hand, the adsorption capacity N_{NH_3} at non-dilute conditions is expected to

1 also be influenced by MOF pore space. Thus, the complete
 2 metric M_{ATS} is expected to be influenced by both MOF
 3 chemistry and textural features. Also note that diffusion
 4 selectivity is an important aspect of choosing a material for a
 5 membrane. This selectivity could be incorporated into the
 6 performance metric (or could be considered in a subsequent
 7 screening step). However, for the purpose of testing the VBO
 8 framework, we decided to focus on the adsorption aspects of
 9 the membrane.

10 **NH₃ capture from air.** NH₃ leakage during storage and
 11 transportation is a persistent risk. The maximum NH₃
 12 concentration that individuals can safely breath for 1h is 1,500
 13 ppm.⁸⁵ One way to mitigate the risk is to accompany storage
 14 and transportation infrastructure with adsorbent traps that can
 15 selectively adsorb substantial amounts of dilute NH₃ over other
 16 molecules in air, including water (Fig. 1c). Preferential NH₃
 17 adsorption over H₂O is most challenging because H₂O is polar
 18 like NH₃, but it would be present at a higher concentration in air.
 19 Thus, we decided to consider a MOF to be potentially useful
 20 only if it is hydrophobic, for which we calculate:

$$21 \quad \delta_{\text{HPHB}} = 1, \text{ if } K_{\text{H}_2\text{O}} \leq 5 \times 10^{-6} \text{ mol kg}^{-1}\text{Pa}^{-1}$$

$$22 \quad \delta_{\text{HPHB}} = 0, \text{ if } K_{\text{H}_2\text{O}} \geq 5 \times 10^{-6} \text{ mol kg}^{-1}\text{Pa}^{-1} \quad (4)$$

23 where $K_{\text{H}_2\text{O}}$ is the adsorption Henry's constant of H₂O at 300 K
 24 and δ_{HPHB} equal to one (zero) indicates that the MOF is
 25 hydrophobic (hydrophilic), in consistency with the $K_{\text{H}_2\text{O}}$
 26 threshold for MOF hydrophobicity determined by Moghadam
 27 *et al.*⁸⁶ Then, we use as performance metric:

$$28 \quad M_{\text{ATSTH}} = M_{\text{ATS}} \times \delta_{\text{HPHB}} \quad (5)$$

29 where M_{ATS} is calculated from Eq. 3 and Eq. 2, with i
 30 corresponding to N₂, O₂ and Ar. Adsorption loadings are
 31 calculated for a N₂/O₂/Ar/NH₃ mixture with $y_{\text{N}_2} = 0.78$, $y_{\text{O}_2} =$
 32 0.21, $y_{\text{Ar}} = 0.0075$ Ar and $y_{\text{NH}_3} = 0.0015$ (i.e., 1500 ppm NH₃)
 33 at 300 K and 1 bar. The above metric circumvents the need to
 34 calculate H₂O adsorption in MOFs, which is known to require
 35 extremely long simulations.⁸⁷ Note that an analogous strategy
 36 to the above was used by Smit and coworkers to discover MOFs
 37 for CO₂ capture from wet flue gas.²⁶ Note that as having enough
 38 space in the MOF pore to store the dilute quantities of NH₃
 39 originally in air is not a concern, MOF performance, and thus
 40 M_{ATSTH} is expected to be primarily influenced by the ability of
 41 the MOF to attract NH₃, and hence by MOF chemistry.

42 3. DIVERSITY-DRIVEN MOF OPTIMIZATION

43 3.1. Workflow overview.

44 An overview of our diversity-driven MOF optimization/search
 45 framework is presented in Fig. 2. To start a MOF (design)
 46 optimization campaign, we randomly draw two MOFs and
 47 calculate their performance metrics using molecular
 48 simulations. These two datapoints are then used to train a
 49 Gaussian Process (GP) regression model⁸⁸ whose kernel is
 50 designed to account for both chemistry and physics (see Section
 51 3.2). The GP is trained to predict the performance metric and
 52 provide the uncertainty associated with the prediction. This
 53 fitted GP is then used to predict the performance of all MOFs
 54 in the hybrid database. From these predictions, our Vendi
 55 Bayesian Optimization (VBO) algorithm selects the next most
 56 promising MOF candidates for which to calculate the
 57 performance metric using molecular simulations.

58 The first candidate that VBO selects is the one
 59 corresponding to the most "optimistic" performance prediction
 60 made by the trained GP. The remaining candidates are selected
 61 only after we prune 10% of the database. The pruning is done
 62 by taking out of the database 10% of the MOFs that, if added to
 63 the set of MOFs previously chosen by VBO and assessed via
 64 molecular simulations, would yield the lowest diversity change
 65 of that set. In our workflow, diversity of a MOF set is calculated
 66 using the Vendi Score (see Section 3.3). The lower the Vendi
 67 score, the lower the diversity of the set. Thus, the MOFs
 68 removed from the database are those that would yield the lowest
 69 Vendi Score if added to the set of MOFs that have been selected
 70 by our VBO algorithm.

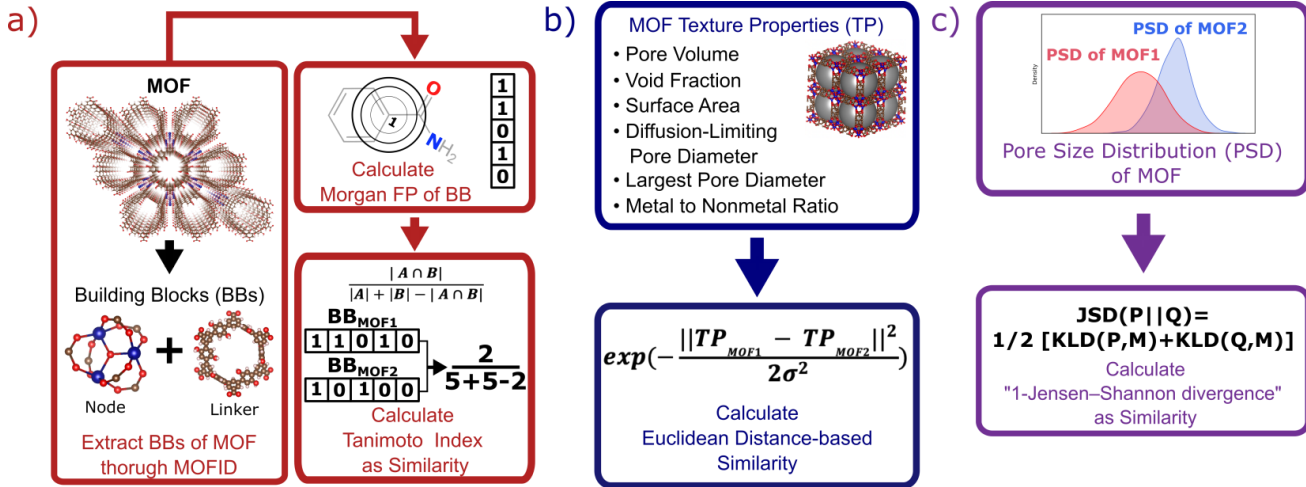
71 Given that for each MOF the GP predicts a distribution
 72 of possible performance metric values, our VBO algorithm uses
 73 the upper confidence bound (UCB) criterion to assess the
 74 "potential" of a MOF. Specifically, the UCB is the mean value
 75 (μ) of the distribution of predictions for the MOF plus two times
 76 the standard deviation (σ). Ideally, upon evaluation with
 77 molecular simulation, some of the MOF selected by our VBO
 78 algorithm should have a higher value of the performance metric
 79 than the MOFs previously evaluated in this same manner.
 80 Regardless, upon completion of the evaluation with molecular
 81 simulation for MOFs that had been selected by the VBO
 82 algorithm, a new GP model is trained leveraging the newly
 83 generated data, and selection of new candidates is done again
 84 using the same procedure as described above. This procedure is
 85 repeated either until a preset target number of iterations is
 86 achieved or the highest value of the performance metric in the
 87 MOFs evaluated with molecular simulation no longer improves.

88 3.2. MOF representation.

89 Each MOF is chemically characterized by the Morgan
 90 fingerprints⁸⁹ of its constituent building blocks (nodes and
 91 linkers), which are extracted from each MOF using MOFid.⁷
 92 MOFid provides the SMILES strings⁹⁰ of the building blocks,
 93 which are used as input for RDKit to provide the fingerprints.
 94 Here, each fingerprint is a vector whose components describe
 95 the atom groups of the corresponding node or linker. Each MOF
 96 is also structurally characterized by its detailed pore size
 97 distribution and global textural properties usually used in the
 98 MOF field. Namely, specific pore volume, void fraction,
 99 specific surface area, largest and diffusion-limiting pore
 100 diameters, and metal-to-nonmetal content ratio. We design a
 101 specific similarity kernel for MOFs. This new kernel is the one
 102 we use for the GP and the calculation of the Vendi Score in our
 103 VBO framework. More specifically, if we denote two different
 104 MOFs by x_1 and x_2 , then the similarity between these MOFs is
 105 given by a specialized kernel function K that is an average of
 106 four different kernels, where each kernel K_i specializes in one
 107 particular aspect of MOFs and is weighted by a factor w_i .
 108 Namely, the kernel similarity between two MOFs x_1 and x_2 is
 109 defined as:

$$110 \quad K(x_1, x_2) = w_1 K_{\text{node}}(x_1, x_2) + w_2 K_{\text{linker}}(x_1, x_2) \\ 111 \quad + w_3 K_{\text{global}}(x_1, x_2) + w_4 K_{\text{PSD}}(x_1, x_2) \quad (6)$$

112 K_{node} and K_{linker} are each a kernel function computing the
 113 Tanimoto similarity⁹¹ between the Morgan fingerprints of either
 114 two nodes or two linkers, respectively (Fig. 3a). The Tanimoto
 115 similarities between Morgan fingerprints have been found to



1

2 **Figure 3.** Schematic representation of methods to calculate kernel similarity between MOFs. a) Chemical similarity (K_{node} and K_{linker} kernels) obtained
 3 by decomposing two MOFs into their building blocks, and calculating the Tanimoto index between the Morgan fingerprints of their building blocks.
 4 b) Global textural properties similarity (K_{global} kernel) obtained by calculating the radial basis function Kernel of the Euclidean distance between the
 5 property vectors of two MOFs. c) Detailed pore structure similarity (K_{PSD} kernel) obtained by calculating the difference between one and the Jensen-
 6 Shannon divergence between the pore size distributions (PSDs) of two MOFs. The different kernels cover different aspects of MOFs, and by tuning
 7 the weights of each Kernel, the representation is adaptable to prediction of properties with different level of dependence on MOF chemistry and
 8 structure.

9 capture important differences in molecule chemistry, and has
 10 been shown effective at guiding machine learning models for
 11 search purposes in other areas.⁹² As a MOF could have more
 12 than one type of node or linker, we do all possible pairwise
 13 comparisons and use the average value of K_{node} or K_{linker} . On the
 14 other hand, K_{global} operates on the global textural properties, and
 15 is defined to be the exponential of the Euclidean distance
 16 between the two vectors containing the (normalized) values of
 17 the above properties for the two MOFs being compared (Fig.
 18 3b). This is analogous to what Simon and coworkers did for
 19 COFs.⁹³ Finally, K_{PSD} is a new kernel proposed by us, which
 20 computes the difference between the pore size distributions
 21 (PSDs) of the two MOFs being compared. We do this by using
 22 the Jensen–Shannon divergence (JSD).⁹⁴ Given two PSDs P
 23 and Q , this function returns:

$$24 \quad JSD(P, Q) = \frac{1}{2}(KLD(P, M) + KLD(Q, M)) \quad (7)$$

25 where $M = \frac{1}{2}(P + Q)$ is a mixture distribution of the original
 26 two P and Q and:

$$27 \quad KLD(P, Q) = \sum_{s \in S} P(s) \log \left(\frac{P(s)}{Q(s)} \right) \quad (8)$$

28 refers to the Kullback–Leibler divergence (KLD) between P and
 29 Q . Here S is the set of possible pore sizes, and $P(s)$ and $Q(s)$
 30 give the probability of a particular pore size s in each of the two
 31 MOFs. JSD computes the distance between the two
 32 distributions, giving a symmetric and bounded metric for their
 33 difference. Our kernel K_{PSD} subsequently calculates the
 34 similarity between the two distributions as $(1 - JSD)$.

35 3.3. Vendi Score.

36 The Vendi score (VS) is key to encourage our optimization
 37 framework to find many diverse solutions, hence avoiding
 38 commitment to a single MOF design “solution” that might be
 39 infeasible to produce and test experimentally. The VS is a
 40 function whose input is the $n \times n$ similarity matrix K
 41 representing data points in a set of size n . The VS is calculated

42 as the exponential of the Shannon entropy of the normalized
 43 eigenvalues of K , denoted by λ_i , as follows:

$$44 \quad VS(K) = \exp \left(- \sum_{i=1}^n \lambda_i \log \lambda_i \right) \quad (9)$$

45 Friedman and Dieng³⁹ showed that the VS is a mathematically
 46 well-defined diversity metric and quantifies the effective
 47 number of unique elements in a set.³⁹ Here, the elements of the
 48 similarity matrix are calculated using Eq. 6, meaning that the
 49 GP model and the VS use the same underlying mathematical
 50 object. To keep the output of the kernel function consistent
 51 across calculations of the VS, we set the weights w_i in Eq. 6 to
 52 all be equal to 0.25. However, note that the weights in Eq. 6
 53 take different values when training the GP model, where they
 54 are optimized for prediction.

55 3.4. Vendi Bayesian optimization (VBO) Framework

56 **Overview.** If MOFs are denoted by x and a MOF database by \mathcal{X} ,
 57 where $x \in \mathcal{X}$, and if f is a “black-box” function that returns the
 58 scalar value of the property or performance metric of interest
 59 (i.e., $f: \mathcal{X} \rightarrow \mathbb{R}$), then we aim to find the MOF x^* that
 60 maximizes the value of the performance metric. More formally,
 61 we find x^* such that:

$$62 \quad x_* = \arg \max_{x \in \mathcal{X}} f(x) \quad (10)$$

63 The above makes f an objective function that models the
 64 mapping between a given MOF and its performance metric.
 65 Here f is approximated by a GP that iteratively improves its
 66 “understanding” of f based on evaluations of f for specific
 67 MOFs x . Here, evaluating $f(x)$ means running molecular
 68 simulations to calculate the relevant performance metric for a
 69 given MOF x . However, our VBO framework is also amenable
 70 to experimental work, where performance metrics are measured
 71 via experiments instead of molecular simulations. In each case,
 72 our VBO framework enables finding the optimal MOF x^* in as

1 few evaluations as possible, to overcome time and/or cost
2 constraints associated with simulations or experiments.

3 **Surrogate model.** The first component of our VBO framework
4 is a surrogate model that expresses a belief about f based on
5 previous evaluations of f —i.e., a belief about the relationship
6 between MOF chemistry/structure and performance. Here, the
7 surrogate model is a GP (see comparison with other models in
8 Section S2), which, as any GP, does not yield a single prediction
9 of f for a given x , but rather a set of predictions that follow a
10 normal (Gaussian) distribution \mathcal{N} such that:

$$11 \quad f(x) \sim \mathcal{N}(\mu, \sigma^2) \quad (11)$$

12 where μ and σ are the mean and the standard deviation of the
13 predictions, respectively. When conditioned on a training set, μ
14 and σ are updated to be the posterior predictive mean and
15 standard deviation, reflecting information learned from the
16 training data. Intuitively, μ and σ represent the value that $f(x)$ is
17 most likely to take and the uncertainty about the predicted μ ,
18 respectively. We refer to Rasmussen and Williams⁸³ for a more
19 thorough treatment of GP learning. To fully specify a GP, one
20 needs a mean value that describes the behavior of f in the
21 absence of data, and a kernel K that calculates similarities
22 between different x ; our choice of K was described in Section
23 3.2. At each iteration of our VBO framework, the values of the
24 performance metric obtained from molecular simulation are
25 normalized so that they range from -1 to 1. (We use the constant
26 zero mean function)., The parameters of the GP model,
27 including the weights w_i in Eq. 6 as well as the mean value and
28 a noise factor, are tuned to maximize the fit to the training data,
29 quantified by the marginal log likelihood of the data, as is
30 standard in Gaussian process modeling.⁸³

31 **Acquisition function.** The second component of our VBO
32 framework is an acquisition function $\alpha(x)$ that guides us
33 towards promising candidate MOFs that are likely to yield high
34 performance and that have not been evaluated). A good
35 acquisition function should balance exploration (learning about
36 how $f(x)$ behaves across the space) and exploitation (zeroing
37 in on high-performance regions). Here, we opt for the Upper
38 Confidence Bound (UCB) function.⁹⁵ UCB adds μ and σ , the
39 mean and standard deviation of the GP prediction, with the
40 latter multiplied by a trade-off factor β , which we set to 2 here:

$$41 \quad \alpha(x) = \mu + 2\sigma. \quad (12)$$

42 This simple expression elegantly captures the balance between
43 exploration of MOFs we are uncertain about (with high σ), and
44 exploitation of MOFs predicted to yield high performance (with
45 high μ). In addition to its interpretability, Taw and Neaton⁹⁶
46 demonstrated good optimization performance of the above
47 acquisition function to optimize methane uptake capacity of
48 MOFs. At each iteration of Bayesian optimization, we find the
49 MOF that maximizes the UCB score to evaluate $f(x)$ with. We
50 repeat this process until our evaluation budget is depleted, each
51 time updating the GP and the UCB score with the newly
52 observed MOFs.

53 **Solution diversification.** Unlike regular Bayesian optimization,
54 VBO iteratively prunes the search space (i.e., the database) by
55 removing remaining candidates that are too similar to those that
56 have been previously selected for evaluation. This removal

57 results in even more exploration than enabled by the acquisition
58 function. Formally, consider a candidate MOF x of unknown
59 performance that we may query. We compute the increase in
60 VS (Δ VS) that we would obtain if we were to evaluate $f(x)$ and
61 add x to the set S containing the MOFs we already selected.
62 That is:

$$63 \quad \Delta VS = VS(S \cup \{x\}) - VS(S) \quad (13)$$

64 If x is different from the data points in S , querying x will add
65 more diversity to our data set, as reflected by a large Δ VS. If,
66 on the other hand, x is similar to the points in S , Δ VS will be
67 small. At each iteration, we compute Δ VS for each of the
68 remaining candidate MOFs, and remove the MOFs that yield
69 the lowest Δ VS until the remaining pool of candidates is
70 reduced by ten percent. We thus reduce the effective search
71 space at each iteration, removing candidates that are too similar
72 to those already acquired.

73 This modification of traditional Bayesian optimization aims at
74 building a diverse set of high-performance MOFs. While this
75 increase level of exploration does not guarantee improved
76 optimization performance, we do not necessarily sacrifice the
77 top MOF either. As the diversity-aware pruning step is reset at
78 each iteration, if we have found a region in our search space that
79 contains very good candidates, our acquisition function allows
80 us to come back to this region (i.e., zeroing in on the top MOF)
81 once other promising regions have been explored. We can also
82 think of this strategy as searching over multiple promising
83 regions at the same time.

84 4. RESULTS AND DISCUSSION

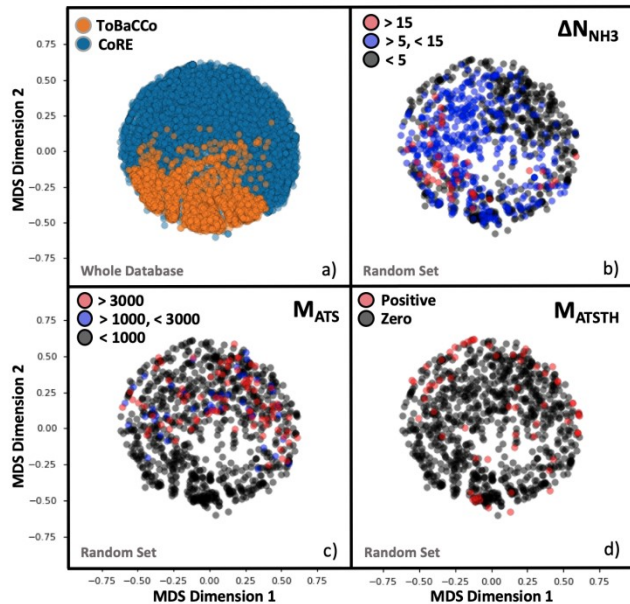
85 4.1. Expressiveness of the MOF-specific kernel.

86 Although the representation of a MOF is inherently
87 multidimensional, the plots in Fig. 4 maps MOFs onto a
88 reduced two-dimensional space, by applying multidimensional
89 scaling (MDS)⁹⁷ to the covariance matrix of the MOFs, which
90 was calculated using the kernel defined earlier by Eq.6. MDS
91 conveys the similarity-dependent original distances between
92 MOFs in multidimensional space, so that in Fig. 4 similar
93 MOFs appear close to each other. From Fig. 4a, the
94 complementary of CoRE MOFs (blue points) and our
95 ToBaCCo MOFs (orange points) is apparent as the groups
96 separate into individual regions. The usual differences between
97 extant CoRE MOFs and hypothesized MOFs such as our
98 ToBaCCo MOF have been pointed out previously in work by
99 others such as Kulik and coworkers.⁵⁴ For instance, CoRE
100 MOFs tend to feature smaller pores and a more diverse
101 selection of metals. ToBaCCo MOFs exhibit a systematic
102 variation in textural properties, focusing on metals Cr, Zr, Mn,
103 Co, Cu, and Zn. Therefore, the observed segregation in Fig. 4a
104 indicates that our kernel captures meaningful
105 similarities/differences between MOFs.

106 Analogously, we present reduced dimensionality plots but only
107 for a random subset of 1,000 MOFs uniformly extracted from
108 the ~10,000 hybrid database, and for which the performance
109 metrics pertinent to NH₃ storage, removal during plasma-
110 assisted synthesis, and capture from air (Δ N<sub>NH₃, M_{ATS} and
111 M_{ATSTH}, respectively) were calculated using molecular
112 simulation. Upon coloring the points based on the value of each
113 performance metric in the corresponding MOF, it is apparent</sub>

1 that segregation also tends to occur on the basis of performance
 2 (Fig. 4b-d). For instance, Fig. 4b shows MOFs with $\Delta N_{NH_3} < 5$
 3 mmol/g locating in an outer ring, MOFs with $5 \text{ mmol/g} < \Delta N_{NH_3}$
 4 $< 15 \text{ mmol/g}$ locating in the inner region, and MOFs with ΔN_{NH_3}
 5 $> 15 \text{ mmol/g}$ locating in a lower-right cluster. Such segregation
 6 indicates how well our measure of similarity (i.e., our kernel) is
 7 conducive to learning.

8 The extent at which our kernel facilitates learning is
 9 illustrated in Fig. 5, which shows parity plots comparing the
 10 prediction of the performance metrics N_{NH_3} , M_{ATS} and M_{ATSTH}

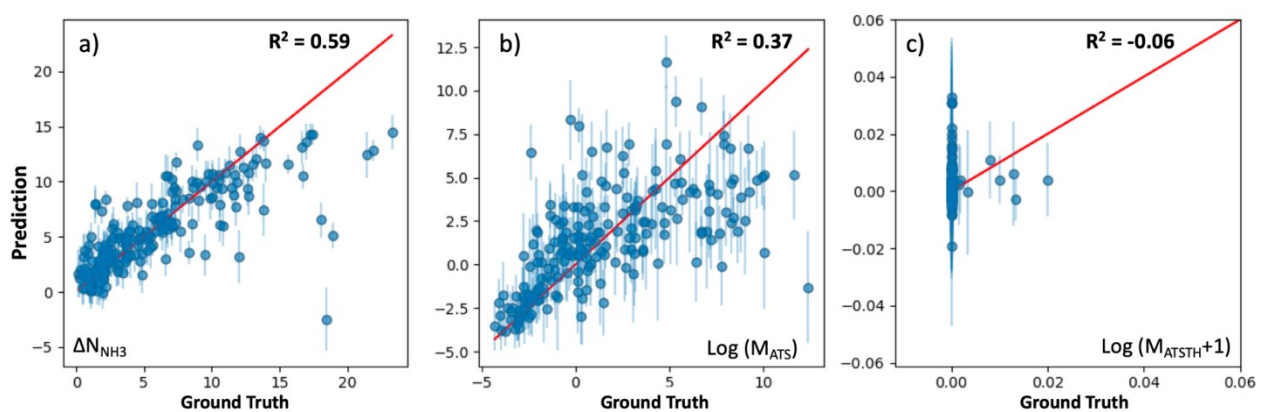


11
 12 **Figure 4.** MOF mapping onto two-dimensional plots by using
 13 multidimensional scaling (MDS) representations. a) all MOFs in the
 14 hybrid database colored by their origin (either the ToBaCCo database

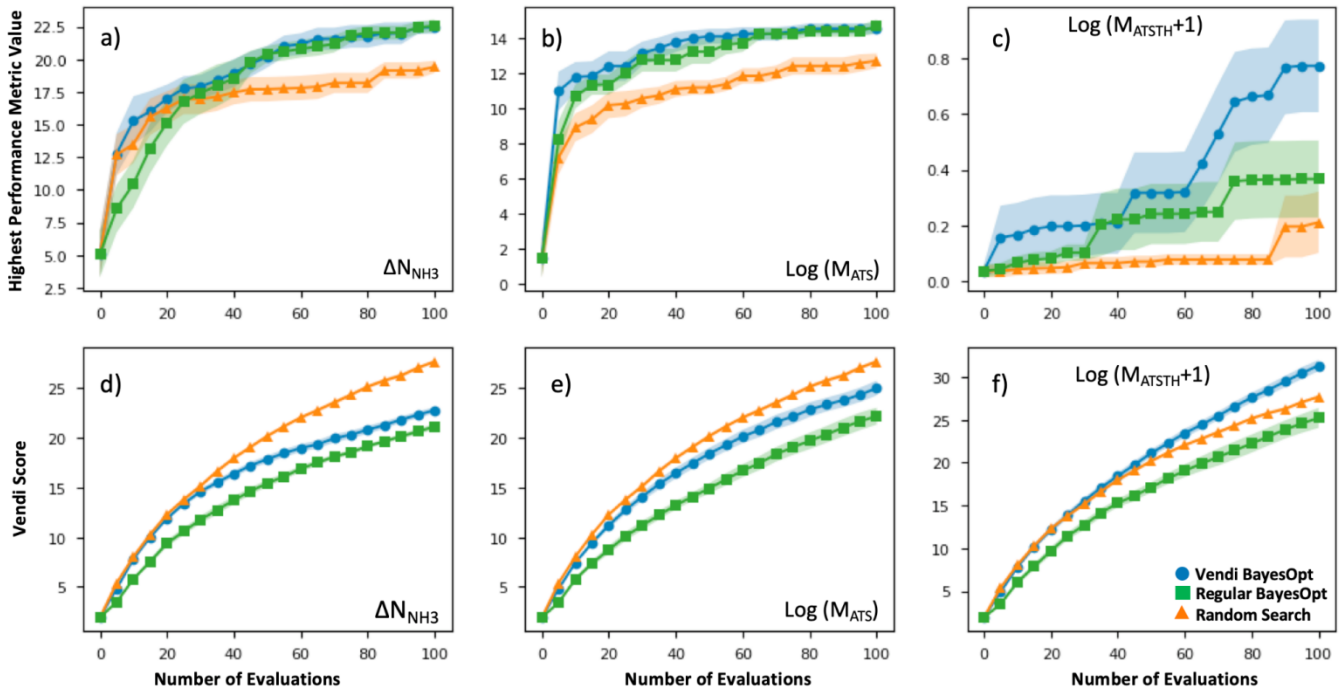
15 or the CoRE database). b-d) 1,000 random MOF subset, colored by
 16 range of ΔN_{NH_3} (b), M_{ATS} (c), and M_{ATSTH} (d) performance metrics.
 17 The extent of segregation observed is a harbinger of the efficacy of our
 18 MOF kernel similarity as input to train the GP.

19 by corresponding GP models trained on molecular simulation
 20 data of the 1,000 random MOF subset. The GPs trained to
 21 predict ΔN_{NH_3} and M_{ATS} (Fig. 5a,b) present relatively similar
 22 correlations between their predictions and the actual values (i.e.,
 23 ground truth) of the corresponding performance metrics.
 24 Namely, R^2 values of 0.59 and 0.37 for ΔN_{NH_3} and M_{ATS} ,
 25 respectively. On the other hand, the GP trained for the M_{ATSTH}
 26 case seems to face higher difficulty in learning to predict the
 27 performance metric, which is reflected by an R^2 value of -0.06
 28 (Fig. 5c). Such difficulty is partly due to the exceptional
 29 roughness of M_{ATSTH} as a function of MOF
 30 chemistry/structure—which partly motivated the selection of
 31 this metric for our testing. The roughness of M_{ATSTH} stems from
 32 the rather binary character of the metric, which is either zero or
 33 positive based on whether the MOF is deemed hydrophobic or
 34 not based on the threshold value of K_{H_2O} , resulting in discrete
 35 changes to M_{ATSTH} that are difficult to capture by machine
 36 learning models. Yet, as we will demonstrate shortly, our VBO
 37 framework remains effective at optimizing these metrics,
 38 including, perhaps surprisingly, M_{ATSTH} .

39 At this point, let us note that the optimized weights (w_i)
 40 for the GP models (Table S3) confirm our hypotheses of what
 41 MOF aspects control performance for each application. For
 42 instance, the chemical similarity kernel K_{node} weighs 0.97 in the
 43 model that predicts M_{ATSTH} but only weighs 0.02 in the model
 44 that predicts ΔN_{NH_3} . By contrast, K_{PSD} weighs 0.37 in the model
 45 that predicts ΔN_{NH_3} , but only weighs 0.01 in the model that
 46 predicts M_{ATSTH} . On the other hand, all kernels weigh rather
 47 similarly in the model that predicts M_{ATS} .



49
 50 **Figure 5.** Prediction performance of GP models (trained on a subset of 1,000 random MOFs extracted from the hybrid database) to predict a) ΔN_{NH_3} ,
 51 b) M_{ATS} , and c) M_{ATSTH} . GP predictions appear on the vertical axis, while the ground truth (from molecular simulation) appears on the horizontal axis.
 52 The parity line is presented in red. Each point represents the prediction for a MOF, with the corresponding error bar representing the uncertainty of the
 53 predictions based on the prediction standard deviation. The observed prediction performance was found on subsequent statistical testing to be sufficient
 54 to make VBO effective.



1

2 **Figure 6.** Efficacy of VBO (blue) applied on a 1,000 subset of random MOFs compared to Bayesian optimization (green) and random search (orange).
3 Top row presents the evolution of the highest value of the performance metric as the number of MOF evaluations increases for a) ΔN_{NH_3} for ammonia
4 storage, b) M_{ATS} for ammonia removal from plasma reactor, and c) M_{ATSTH} for ammonia capture from air. Bottom row presents the evolution of the
5 Vendi Score for the set of evaluated MOFs as the number of MOF evaluations increases for d) ΔN_{NH_3} for ammonia storage, e) M_{ATS} for ammonia
6 removal from plasma reactor, and f) M_{ATSTH} for ammonia capture from air. Results in a)-f) are averaged across 10 repeat runs, the average value is
7 indicated by the solid line, whereas the standard deviation is indicated by the shaded area. Both VBO and Bayesian optimization outperformed random
8 search, but VBO provided higher diversity of MOF “solutions.”

9 4.2. Statistical testing of VBO efficacy.

10 The efficacy of VBO was statistically assessed by simulating
11 our workflow (Fig. 2) ten times on the subset of randomly
12 selected 1,000 MOFs, to iteratively optimize MOF design for
13 the ΔN_{NH_3} , M_{ATS} and M_{ATSTH} metrics. During each run, two
14 MOFs were randomly selected to be the initial training set, and
15 100 MOFs were evaluated in 20 batches of five MOFs each
16 iteration (i.e., when 10% of the MOF subset was evaluated, the
17 run stopped). Each time our VBO workflow was run, an
18 analogous run without the Vendi score-based pruning (i.e., a
19 regular Bayes optimization run) was done in parallel for
20 comparison, as well as random search consisting of the
21 evaluation of 100 randomly selected MOFs within the subset.
22 The lines in Fig. 6 present the average progress of the VBO
23 (blue), Bayesian optimization (green) and random search
24 (orange) runs, whereas the corresponding shaded areas
25 represent the corresponding standard errors.

26 As evidenced by Fig. 6, although the uncertainty
27 region for VBO and Bayesian optimization tend to overlap, on
28 average VBO did equal or better than Bayesian optimization,
29 when assessed based on the highest value for the metric
30 encountered by the end of 100 evaluations. Notably, VBO
31 outperformed Bayesian optimization for the evaluation of the
32 M_{ATSTH} metric for NH_3 capture from air. On the other hand,
33 both VBO and Bayesian optimization clearly do better on
34 average than random search when compared by the
35 abovementioned criterion. Furthermore, the uncertainty regions
36 for the latter two methods and random search barely overlap,
37 suggesting that in a worst-case scenario VBO and Bayesian

38 optimization would do at least as well as a best-case scenario
39 random search that explores ten percent of the available design
40 space.

41 But the most significant difference between VBO and
42 Bayesian optimization is the more diverse exploration of the
43 design space by VBO. This fact is evidenced by the consistently
44 higher Vendi score among evaluated MOFs as VBO progresses
45 compared to Bayesian optimization. As expected, random
46 search tends to result in the highest diversity among evaluated
47 MOFs as the search progresses. But it is surprising that for the
48 optimization of M_{ATSTH} our VBO ended up on average with a
49 higher diversity of evaluated MOFs than random search.
50 Ultimately, the average behavior of the Vendi Score in VBO
51 versus Bayesian optimization is indicative that VBO is bound
52 to create a more diverse pool of promising MOFs for a given
53 application.

54 4.3. Full database search for MOFs for NH_3 storage.

55 Encouraged by the statistical efficacy of our VBO framework,
56 we decided to perform a full VBO run on the complete hybrid
57 database (i.e., ~10,000 MOFs) to optimize ΔN_{NH_3} . Specifically,
58 to find MOFs with potential for NH_3 storage, considering
59 storage at 1 bar with storage/release through a 300 K to 400 K
60 thermal swing. Fig. 7a presents the progress of the performed
61 VBO run of 20 iterations (each iteration corresponds to a batch
62 of 20 MOFs), comparing it against a random search (technically
63 consisting of the previously randomly selected 1,000 MOFs on
64 which VBO was previously tested in Section 4.2). Evidently,
65 VBO greatly outperforms random search, with the former
66 identifying MOFs with ΔN_{NH_3} values approaching as high as 30

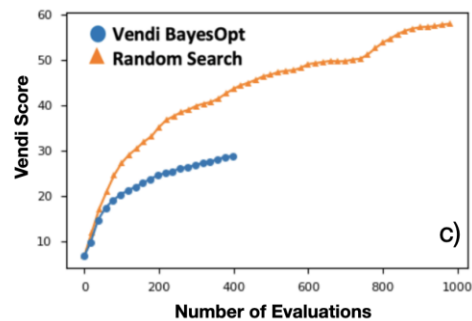
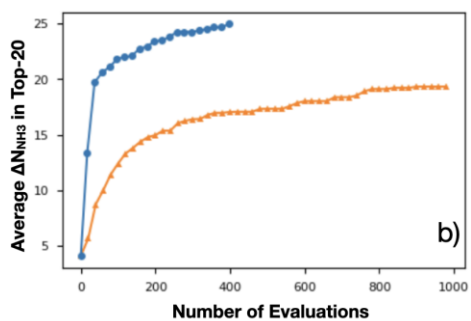
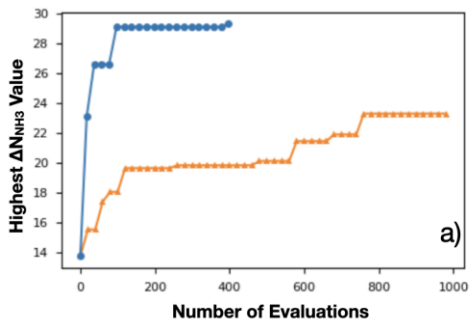
1 $\text{mmol}_{\text{NH}_3}/\text{gMOF}$, whereas the latter did not identify MOFs with
2 ΔN_{NH_3} values higher than $\sim 23 \text{ mmol}_{\text{NH}_3}/\text{gMOF}$.

3 Notably, the outperformance of VBO relative to
4 random search occurred despite VBO terminating early at ca.
5 400 evaluations. This early termination was made because the
6 highest ΔN_{NH_3} value within the evaluated MOFs did not change
7 significantly after around 80 evaluations. However, note that
8 one should not be tempted to consider subsequent MOF
9 evaluations after the 80th evaluation point as wasteful, as these
10 evaluations enabled to strengthen the pool of promising MOF
11 designs for NH_3 storage. A fact that is evidenced by the steady
12 improvement in the average ΔN_{NH_3} for the “top-20” evaluated
13 MOFs from the 80th to the 400th evaluation (Fig. 7b).
14 Importantly, this improvement in average ΔN_{NH_3} was
15 accomplished while steadily improving the diversity of the
16 evaluated MOF as indicated by the steady improvement in the
17 Vendi score within the same range of evaluations (Fig. 7c). The
18 latter creates confidence that the pool of promising MOFs to be
19 suggested for future synthesis and experimental testing to be
20 more diverse than provided by other methods.

21 4.4. Data-driven MOF design rules

22 As noted earlier, a benefit of computational MOF screening is
23 the emergence of structure-performance relationships, which
24 are useful to establish design rules that experimentalists could
25 leverage to conceive adsorbent designs of their own (not even
26 necessarily for MOFs). Importantly, the emergence of these
27 relationships allows extracting value from computational
28 screenings independently of the success in synthesizing and
29 testing the specific MOF designs recommended by the
30 screening. However, the nature of the emerging relationships is
31 empirical, and thus depend on a sufficiently large number of
32 observations being made to create clear trends. Conveniently,
33 here, while the number of evaluated MOFs is lower than in
34 other screening studies that relied on exhaustive search, the bias
35 of our selection method towards “good” MOFs allow us to still
36 define well the “interesting” region of the relationship relevant
37 to optimize the performance metric of interest.

77



78

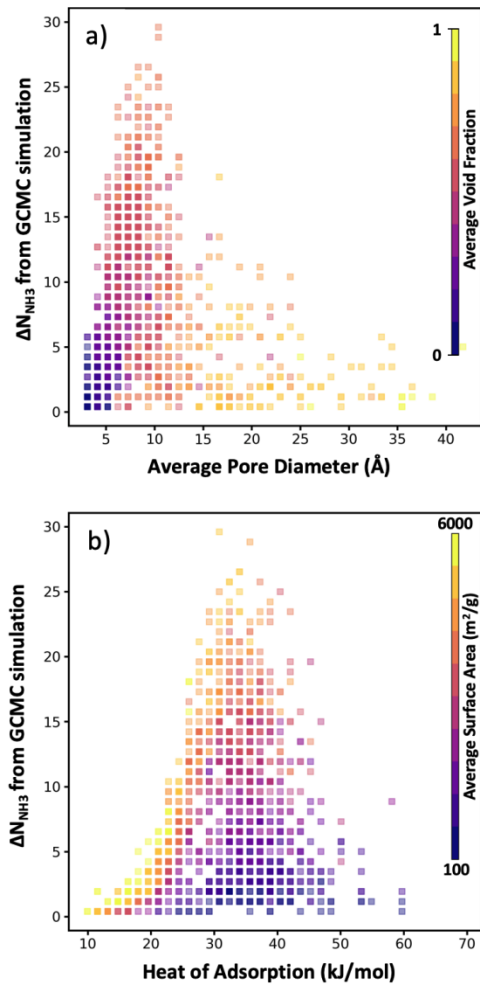
79 **Figure 7.** Evolution of VBO campaign (blue) in the $\sim 10,000$ MOF database, when searching for MOFs for NH_3 storage, compared to the evolution
80 of the random search (orange). a) Evolution of the highest ΔN_{NH_3} found among evaluated MOFs at a given point in the campaign. b) Evolution of the
81 average ΔN_{NH_3} among the top-20 evaluated MOFs at a given point in the campaign. c) Evolution of the Vendi Score of evaluated MOFs at a given
82 point in the campaign. Note that the VBO campaign was ended early due to negligible changes in the highest ΔN_{NH_3} since the 80th evaluation. Once
83 again VBO greatly outperformed random search.

84

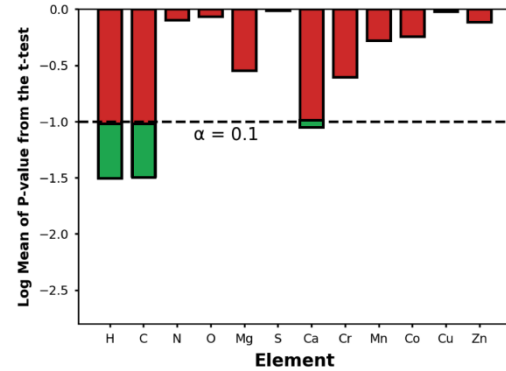
38 For instance, although in Fig. 8a there is a dearth of data for
39 MOFs with average pore diameter (APD) larger than 14 \AA , it is
40 apparent that the optimal average pore diameter and for NH_3
41 storage at the conditions herein proposed is 10 \AA . Note that the
42 scarcity of data for MOFs with APD larger than 14 \AA is due to
43 reluctance by the VBO algorithm to pick MOFs in that range of
44 APD, probably due to rapidly learning that APDs larger than 14
45 \AA tend not to optimize ΔN_{NH_3} . An APD of 10 \AA seems to
46 compromise confinement effects (i.e., overlap of interaction
47 potentials) to enhance NH_3 attraction to the pore walls and
48 having sufficient space to accommodate NH_3 molecules. To be
49 sure, an APD of 10 \AA should be interpreted as necessary, and
50 not as a sufficient condition to optimize ΔN_{NH_3} , as evidenced by
51 the wide range of ΔN_{NH_3} values that can be observed for that
52 APD value. The color coding in Fig. 8a suggests that such
53 variability in ΔN_{NH_3} at APD equal to 10 \AA is *partly* explained
54 by variations in MOF void fraction—with MOFs with void
55 fraction around 0.7 tending to appear at the top. In other words,
56 given two MOFs with APD equal to 10 \AA , the one with higher
57 void fraction probably corresponds to a higher ΔN_{NH_3} , again
58 partly due to the implication that higher void fraction allows
59 more space to accommodate NH_3 molecules.

60 On the other hand, note that while attraction of NH_3 to
61 the pore walls (as reflected by the heat of adsorption Q_{st}) is
62 desired, too strong an attraction is detrimental to ΔN_{NH_3} as it
63 prevents the adsorbed NH_3 molecules to be easily released.
64 From our collected data, it seems that a Q_{st} of 33 kJ/mol is
65 optimal for ammonia storage at the conditions herein proposed
66 (Fig. 8b). Analogous to our APD analysis, a Q_{st} of 33 kJ/mol
67 should be taken only as a necessary but not sufficient condition
68 to optimize ΔN_{NH_3} . Indeed, there is a wide range of ΔN_{NH_3}
69 values at Q_{st} equal 33 kJ/mol . The color coding in Fig. 8b partly
70 explains this variability on the basis of surface area variations—
71 with MOFs with surface area around $4000 \text{ m}^2/\text{g}$ tending to
72 appear at the top, as they provide a larger number of sites with
73 optimal interaction strength. Note that inspecting Fig. S6, it
74 seems that a Q_{st} value around 33 kJ/mol enables recovering up
75 to 95 % of the NH_3 molecules adsorbed at the storage conditions

76



1
2 **Figure 8.** Plots of structure-performance relationships for NH₃ storage.
3 Each square bin corresponds to a combination of the ΔN_{NH_3}
4 performance metric and MOF property, where the transparency of
5 each square bin is indicative of the number of MOFs in the bin, and
6 the color of each bin reflects the average value of the property in the
7 side color scale across all MOFs in the bin. a) ΔN_{NH_3} versus MOF
8 average pore diameter (APD), with each bin colored by MOF void
9 fraction. b) ΔN_{NH_3} versus heat of adsorption Q_{st} , with each bin colored
10 by gravimetric surface area. Optimal APD and Q_{st} appears to be 10 Å
11 and 33 kJ/mol, respectively.



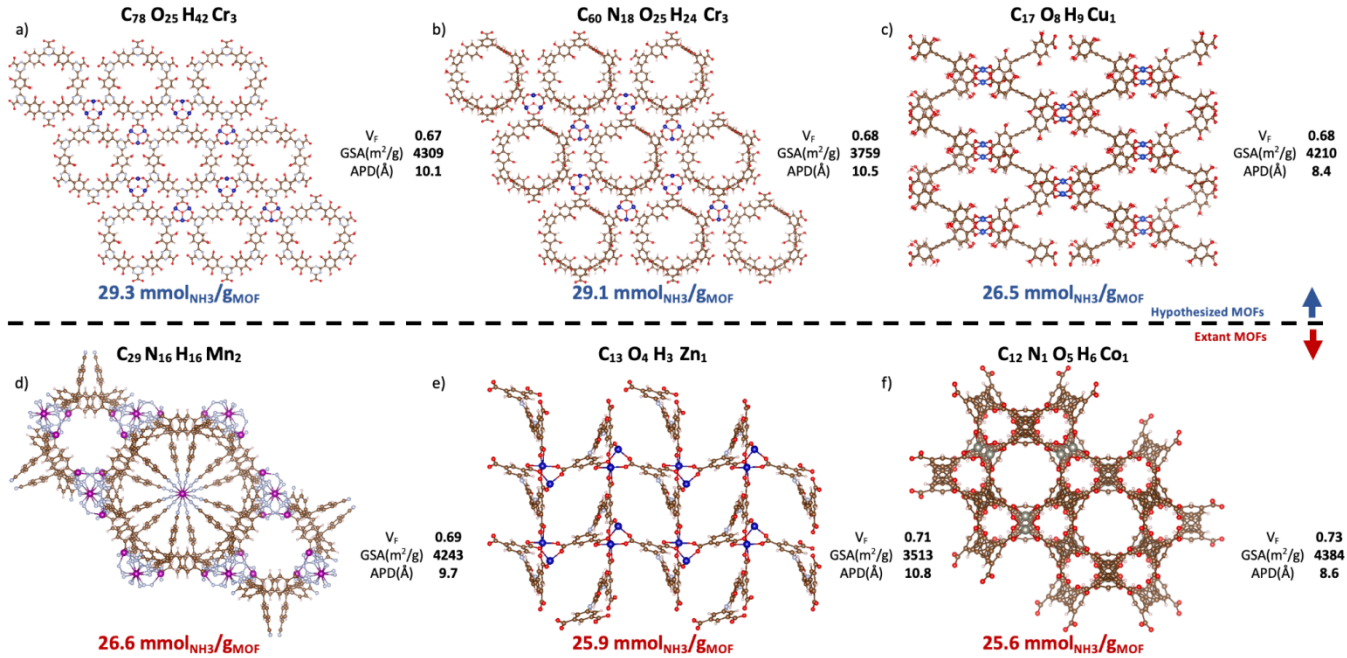
12
13 **Figure 9.** Statistical significance for comparison of elemental
14 compositions between the top-14 MOFs and the entire database based
15 on the p-values derived from the t-test. The dashed line represents our
16 chosen critical value for the one-sided t-test. Bars that fall below this
17 threshold indicate elements that are statistically significantly more
18 abundant in the top-performing MOFs. Ca is a metal that appears
19 significantly more frequently in the top-14 MOFs than in the full
20 database.

21 We acknowledge, however, that a design rule centered
22 around Q_{st} is somewhat abstract as this quantity does not depend
23 only on MOF chemistry, but also on MOF structure. In an
24 attempt to provide some chemistry-based MOF design rules for
25 NH₃ storage, we decided to explore trends in elemental
26 composition among outstanding MOFs. Specifically, for each
27 element in the periodic table, we calculated its average percent
28 content in the top-14 MOFs evaluated with molecular
29 simulation and compared this value with the corresponding
30 average percent content in all ~10,000 MOFs in the database
31 (Fig. S7). Then we used a t-test to assess the statistical
32 significance of observed differences.

33 **Fig. 9** shows the p-values for the t-test for the elements
34 present in the top-14 MOFs. Using a p-value threshold of 0.1,
35 it seems that C, H, and Ca are elements that are, with statistical
36 significance, more abundant within the top-14 MOFs for NH₃
37 storage than in MOFs at large. Using our understanding of
38 MOF structure, we rationalize that the higher abundance of C,
39 H is probably just a reflection of the optimal APD for ammonia
40 storage being larger than the median APD in the database—i.e.,
41 larger pores imply longer linkers, hence more C and H content.
42 On the other hand, we could not find an alternative explanation
43 for the higher abundance of Ca within the outstanding MOFs,
44 suggesting a primarily chemical effect—after all, CaCl₂ is a
45 popular ammonia adsorbent.⁹⁸ To be sure, though, due to the

46

47

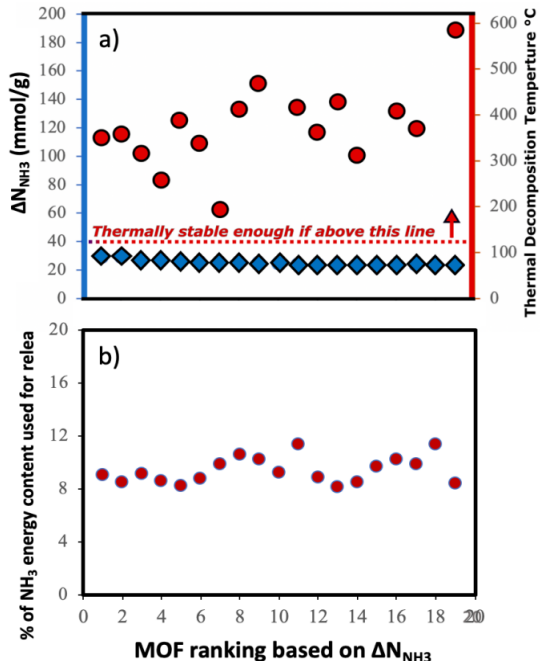


2 **Figure 10.** Top-6 MOFs ranked by ΔN_{NH_3} value. Hypothesized and extant MOFs are in the top and bottom rows, respectively. V_f , GSA, and APD
3 represent, respectively, the void fraction, gravimetric surface areas, and average pore diameter from pore size distribution. The CSD refcode and
4 corresponding publication can be found in [Table S5](#). The three hypothesized MOFs are potentially synthesizable per the free energy criterion by
5 Anderson and Gómez-Gualdrón ([Table S6](#)).⁵⁴ Ca MOFs appear in the top-14 but not in top-6 presumably due to suboptimal textural properties.

6

18 4.5. Promising MOF designs.

19 Contingent on adsorption simulation accuracy, now we proceed
20 to present some promising MOF designs identified by our VBO
21 run. The top-20 MOFs are listed in [Table S4](#), while the top-6
22 MOFs are presented in [Fig. 10](#). Three of these MOFs
23 correspond to hypothesized designs (top row), and the
24 remaining three correspond to extant designs that have been
25 realized synthetically (bottom row). The free energy of the
26 hypothesized designs in [Fig. 10](#) was calculated using the
27 Frenkel-Ladd method as discussed in earlier work,⁹⁹ resulting
28 in free energies below 4.4 kJ/mol per atom, which per
29 discussion in ref.¹⁰⁰ suggests high synthesizability likelihood.
30 The MOFs in [Fig. 10](#) present ΔN_{NH_3} values in the 26.6-
31 29.3 $mmol_{NH_3}/g_{MOF}$. Consistent with observed structure-
32 performance relationships (Section 4.4), these MOFs exhibit
33 APDs around 10 \AA , void fractions around 0.7 and surface areas
34 around 3900 m^2/g . As for metals, note that although Ca was
35 more abundant in the top-14 MOFs than in the whole database,
36 the six best MOF designs featured Cr, Cu, Mn, Zn, and Co
37 instead. Probably, because the textural properties of Ca MOFs
38 were not “ideal.” This situation underscores the importance of
39 optimizing a MOF design *both* structurally and chemically.



7
8 **Figure 11.** a) Thermal stability in top-20 MOFs from VBO campaign.
9 Blue diamonds indicate ΔN_{NH_3} (left-axis) and red circles indicate
10 predicted thermal decomposition temperature (right-axis). Top-20
11 MOFs appear likely to withstand operation conditions. b) Estimated
12 energy penalty to release stored NH_3 as percentage of the hydrogen-
13 based energy content of NH_3 (22.5 MJ/kg NH_3) in the top-20 MOFs.
14 Penalty hovers around 8 to 12 percent on NH_3 energy content.

15 role other MOF features play on ΔN_{NH_3} , the presence of Ca
16 alone, as we will see below, does not guarantee the
17 maximization of ΔN_{NH_3} .

40 To put the predicted ΔN_{NH_3} for MOFs in [Fig. 10](#) in the
41 context of other MOFs experimentally tested in the literature,
42 first let us reiterate that while NH_3 adsorption in MOFs have
43 been consistently evaluated considering 300 K and 1 bar as the
44 storage condition, such consistency has not existed for the
45 release condition. Thus, a direct comparison is not possible.
46 However, note that, with the exception of LiCL-MIL-53, the
47 highest reported NH_3 loading at 300 K and 1 bar is 23.9
48 $mmol_{NH_3}/g_{MOF}$, so that even assuming total recovery at the
49 release conditions, the predicted ΔN_{NH_3} for the MOFs in [Fig. 10](#)

1 is still higher. As for LiCl-MIL-53, its measured 33.9
 2 mmol_{NH₃}/gMOF loading at 300 K and 1 bar is accompanied by a
 3 reported Q_{st} around 78 kJ/mol.⁵¹ Based on the relationship
 4 between heat of adsorption and percent NH₃ recovered (Fig. S6)
 5 emerged in the study herein, a best case scenario for this Q_{st} (i.e.,
 6 50 % recovery) would yield a ΔN_{NH_3} around 16.9 mmol_{NH₃}/gMOF
 7 for this MOF, which again is below the predicted ΔN_{NH_3} for the
 8 MOFs in Fig. 10.

9 Although here we focused on optimizing the MOF
 10 design to maximize ΔN_{NH_3} , other factors also play a role when
 11 using a MOF for a given application. Considering that we
 12 propose a thermal swing to release NH₃, it is important to assess
 13 the thermal stability of the MOFs to encourage experimental
 14 testing. Accordingly, in Fig. 11a, we show the thermal
 15 decomposition temperature T_d of each of the top-20 MOFs
 16 (ΔN_{NH_3} ranging from 23 to 30 mmol_{NH₃}/gMOF), as predicted by
 17 an ANN model developed by Nandy *et al.*,¹⁰¹ as available in the
 18 MOFsimplify website.¹⁰² This model makes the prediction
 19 based on the revised autocorrelation (RAC) descriptors of the
 20 MOFs, and was trained using reported thermogravimetric
 21 analysis (TGA) data for 3,131 MOFs, with a mean absolute
 22 error (MAE) of 47 K. Considering this MAE and that the lowest
 23 predicted T_d was 466 K (which is 66 K higher than the upper
 24 temperature for the thermal swing), it seems that the suggested
 25 MOF designs are likely to withstand the proposed operation
 26 conditions.

27 Finally, to inform considerations about energy
 28 efficiency and economic viability, we estimated the energy
 29 required to release each kilogram of stored NH₃ with the
 30 proposed thermal swing, $\Delta Q_{release}$, using:

$$31 \quad \Delta Q_{release} = Q_{st} + (Cp_{NH_3} + \frac{Cp_{MOF}}{\Delta N_{NH_3}}) \times \Delta T \quad (14)$$

32 Where, again, Q_{st} is the heat of adsorption of NH₃, Cp_{NH_3} is the
 33 heat capacity of NH₃ in the gas phase (2.2 kJ/kg_{NH₃}-K), Cp_{MOF}
 34 is the heat capacity of the MOF, and ΔT is the thermal swing
 35 magnitude (100 K). Eq 14 is analogous to that used by Smit and
 36 coworkers to estimate the energy to release captured CO₂ from
 37 MOFs,²⁶ and essentially accounts for the heating of the MOF
 38 along with adsorbed NH₃ molecules from 300 K to 400 K, plus
 39 the energy needed to desorb NH₃ from the MOF at 400 K. For
 40 all MOFs, we used the average Cp_{MOF} value (0.87 kJ/kg_{MOF}-K)
 41 previously reported for eleven MOFs,^{103,104} considering that
 42 this property seems to have low variability among MOFs.

43 Assuming that the energy stored in NH₃ corresponds
 44 to that of the H₂ that is released from NH₃ via cracking, the
 45 energy content of NH₃ is 22.5 MJ/kg_{NH₃}.¹⁰⁵ The latter implies
 46 that with the proposed MOF designs a penalty between 8 % and
 47 12 % of the NH₃ energy content would be used to release the
 48 stored NH₃. For context, an analogous calculation can be done
 49 to estimate energy penalty for liquid NH₃ storage, which can be
 50 estimated based on the latent heat of condensation for NH₃ (1.4
 51 MJ/kg_{NH₃})¹⁰⁶ and the energy to cool down NH₃ from 300 K
 52 down to 240 K. The above results in an estimated penalty of 7%
 53 of the NH₃ energy content. Considering that adsorptive NH₃
 54 storage at ambient conditions can bypass other technological
 55 requirements such as insulation, toxicity, corrosion, or issues
 56 such as boil-off,^{43,45} among others, the operation conditions

57 proposed herein for adsorptive NH₃ storage (and materials to
 58 achieve so) seem to merit reasonable consideration.

59 5. CONCLUSIONS

60 In this work, we developed a novel framework for efficiently
 61 finding a diverse set of optimal MOFs for applications
 62 involving ammonia adsorption. Our framework, called Vendi
 63 Bayesian Optimization (VBO), seamlessly combines traditional
 64 Bayesian optimization with the Vendi Score, a diversity
 65 measure rooted in ecology and quantum mechanics. VBO is
 66 also made possible by the introduction of a novel similarity
 67 function in the space of MOFs that accounts for both chemistry
 68 and structure. We used this similarity function both for the GP
 69 used by Bayesian optimization and to compute the Vendi Score.
 70 Our framework enabled the efficient discovery of several
 71 optimal MOFs that are distinct from one another, and that
 72 perform better than MOFs previously studied experimentally
 73 for NH₃ storage. Our analysis of the results of VBO highlights
 74 new design rules that MOF experimentalists can leverage to
 75 design optimal MOFs for the above application. We believe
 76 VBO introduces new useful capabilities for the efficient
 77 exploration of the combinatorially large MOF design space for
 78 the discovery of MOFs with desired properties. Importantly,
 79 our VBO framework is amenable to applications beyond
 80 ammonia adsorption. We leave the exploration of these
 81 applications as future work.

82 SUPPLEMENTARY INFORMATION

83 Force field details, details on surrogate model selection,
 84 additional details on VBO campaigns, additional structure-
 85 property relationships, additional details about promising MOF
 86 designs for NH₃ storage.

87 DATA AVAILABILITY

88 Code to replicate our results can be freely accessed at
 89 <https://github.com/vertaix/VBO>. Data sources are available
 90 at
 91 <https://wustl.box.com/s/3jrz8ksu9l3d1hqikir4olainke9wc5t>
 92 and Jupyter notebooks to reproduce our figures are available at
 93 <https://github.com/vertaix/VBO/tree/main/notebooks/Recr>
 94 [eate%20figures](https://github.com/vertaix/VBO/tree/main/notebooks/Recr).

95 ACKNOWLEDGEMENTS

96 D.A.G.-G and A.B.-D. acknowledge funding from the National
 97 Science Foundation through grant OAC-2118201 (HDR:
 98 Institute for Data-Driven Dynamic Design). A.B.-D.
 99 acknowledges Schmidt Sciences for the AI2050 Early Career
 100 Fellowship. Molecular simulations were possible thanks to the
 101 Mio supercomputer cluster at the Colorado School of Mines.

102 AUTHOR CONTRIBUTIONS

103 D.A.G.G and A.B.D designed, supervised and acquired funding
 104 for the project. T.-W.L. and Q.N conducted the work under
 105 D.A.G.G and A.B.D. supervision. T.-W.L primarily focused on
 106 materials selection and characterization, data acquisition via
 107 molecular simulation, and analysis of simulation data in the
 108 context of target applications. Q.N. primarily focused on
 109 building the machine learning model and designing the search

1 algorithm. D.A.G-G. led the manuscript writing. All authors
2 participated in discussions and intellectually contributed during
3 the progress of the project. All authors edited and contributed
4 to the editing of the manuscript and agreed on its final version.

5 REFERENCES

6

7 (1) Gomez-Gualdrón, D. A.; Gutov, O. V.; Krungleviciute, V.;
8 Borah, B.; Mondloch, J. E.; Hupp, J. T.; Yildirim, T.; Farha, O.
9 K.; Snurr, R. Q. Computational design of metal–organic
10 frameworks based on stable zirconium building units for storage
11 and delivery of methane. *Chem. Mater.* **2014**, *26*, 5632–5639.

12 (2) Zheng, J.; Tian, J.; Wu, D.; Gu, M.; Xu, W.; Wang, C.; Gao, F.;
13 Engelhard, M. H.; Zhang, J.-G.; Liu, J.; et al. Lewis acid-base
14 interactions between polysulfides and metal organic framework
15 in lithium sulfur batteries. *Nano Lett.* **2014**, *14*, 2345–2352.

16 (3) Gómez-Gualdrón, D. A.; Colón, Y. J.; Zhang, X.; Wang, T. C.;
17 Chen, Y.-S.; Hupp, J. T.; Yildirim, T.; Farha, O. K.; Zhang, J.;
18 Snurr, R. Q. Evaluating topologically diverse metal–organic
19 frameworks for cryo-adsorbed hydrogen storage. *Energy*
20 *Environ. Sci.* **2016**, *9*, 3279–3289.

21 (4) Zhao, X.; Liu, S.; Tang, Z.; Niu, H.; Cai, Y.; Meng, W.; Wu, F.;
22 Giesy, J. P. Synthesis of magnetic metal–organic framework
23 (MOF) for efficient removal of organic dyes from water. *Sci. Rep.* **2015**, *5*, 11849.

24 (5) Kirchon, A.; Feng, L.; Drake, H. F.; Joseph, E. A.; Zhou, H.-C.
25 From fundamentals to applications: a toolbox for robust and
26 multifunctional MOF materials. *Chem. Soc. Rev.* **2018**, *47*,
27 8611–8638.

28 (6) Anderson, R.; Gómez-Gualdrón, D. A. Increasing topological
29 diversity during computational “synthesis” of porous crystals:
30 how and why. *CrystEngComm* **2019**, *21*, 1653–1665.

31 (7) Bucior, B. J.; Rosen, A. S.; Haranczyk, M.; Yao, Z.; Ziebel, M.
32 E.; Farha, O. K.; Hupp, J. T.; Siepmann, J. I.; Aspuru-Guzik, A.;
33 Snurr, R. Q. Identification schemes for metal–organic
34 frameworks to enable rapid search and cheminformatics analysis.
35 *Cryst. Growth Des.* **2019**, *19*, 6682–6697.

36 (8) O’Keffe, M.; Peskov, M. A.; Ramsden, S. J.; Yaghi, O. M. The
37 Reticular Chemistry Structure Resource (RCSR) database of, and
38 symbols for, crystal nets. *Acc. Chem. Res.* **2008**, *41*, 1782–1789.

39 (9) Islamov, M.; Babaei, H.; Anderson, R.; Sezginel, K. B.; Long, J.
40 R.; McGaughey, A. J. H.; Gomez-Gualdrón, D. A.; Wilmer, C.
41 E. High-throughput screening of hypothetical metal–organic
42 frameworks for thermal conductivity. *npj Comput. Mater.* **2023**,
43 *9*, 11.

44 (10) Colón, Y. J.; Snurr, R. Q. High-throughput computational
45 screening of metal–organic frameworks. *Chem. Soc. Rev.* **2014**,
46 *43*, 5735–5749.

47 (11) Ahmed, A.; Seth, S.; Purewal, J.; Wong-Foy, A. G.; Veenstra,
48 M.; Matzger, A. J.; Siegel, D. J. Exceptional hydrogen storage
49 achieved by screening nearly half a million metal–organic
50 frameworks. *Nat. Commun.* **2019**, *10*, 1568.

51 (12) Jain, A.; Ong, S. P.; Hautier, G.; Chen, W.; Richards, W. D.;
52 Dacek, S.; Cholia, S.; Gunter, D.; Skinner, D.; Ceder, G.; et al.
53 Commentary: The Materials Project: A materials genome
54 approach to accelerating materials innovation. *APL Mater.* **2013**,
55 *1*, 011002.

56 (13) Simon, C. M.; Kim, J.; Gomez-Gualdrón, D. A.; Camp, J. S.;
57 Chung, Y. G.; Martin, R. L.; Mercado, R.; Deem, M. W.; Gunter,
58 D.; Haranczyk, M.; et al. The materials genome in action:
59 identifying the performance limits for methane storage. *Energy*
60 *Environ. Sci.* **2015**, *8*, 1190–1199.

61 (14) Chung, Y. G.; Haldoupis, E.; Bucior, B. J.; Haranczyk, M.; Lee,
62 S.; Zhang, H.; Vogiatzis, K. D.; Milisavljevic, M.; Ling, S.;
63 Camp, J. S.; et al. Advances, Updates, and Analytics for the
64 Computation-Ready, Experimental Metal–Organic Framework
65 Database: CoRE MOF 2019. *J. Chem. Eng. Data* **2019**, *64*,
66 5985–5998.

67 (15) Wilmer, C. E.; Leaf, M.; Lee, C. Y.; Farha, O. K.; Hauser, B. G.;
Hupp, J. T.; Snurr, R. Q. Large-scale screening of hypothetical
metal–organic frameworks. *Nat. Chem.* **2011**, *4*, 83–89.

68 (16) Addicoat, M. A.; Coupry, D. E.; Heine, T. AuToGraFS:
69 automatic topological generator for framework structures. *J.
70 Phys. Chem. A* **2014**, *118*, 9607–9614.

71 (17) Bureekaew, S.; Schmid, R. Hypothetical 3D-periodic covalent
72 organic frameworks: exploring the possibilities by a first
73 principles derived force field. *CrystEngComm* **2013**, *15*, 1551.

74 (18) Moghadam, P. Z.; Li, A.; Wiggins, S. B.; Tao, A.; Maloney, A. G.
75 P.; Wood, P. A.; Ward, S. C.; Fairén-Jimenez, D. Development
76 of a cambridge structural database subset: A collection of metal–
77 organic frameworks for past, present, and future. *Chem. Mater.*
78 **2017**, *29*, 2618–2625.

79 (19) Colón, Y. J.; Gómez-Gualdrón, D. A.; Snurr, R. Q. Topologically
80 Guided, Automated Construction of Metal–Organic Frameworks
81 and Their Evaluation for Energy-Related Applications. *Cryst.
82 Growth Des.* **2017**, *17*, 5801–5810.

83 (20) Burner, J.; Luo, J.; White, A.; Mirmiran, A.; Kwon, O.; Boyd, P.
84 G.; Maley, S.; Gibaldi, M.; Simrod, S.; Ogden, V.; et al. ARC–
85 MOF: A Diverse Database of Metal–Organic Frameworks with
86 DFT-Derived Partial Atomic Charges and Descriptors for
87 Machine Learning. *Chem. Mater.* **2023**, *35*, 900–916.

88 (21) Lee, S.; Kim, B.; Cho, H.; Lee, H.; Lee, S. Y.; Cho, E. S.; Kim, J.
89 Computational Screening of Trillions of Metal–Organic
90 Frameworks for High-Performance Methane Storage. *ACS Appl.
91 Mater. Interfaces* **2021**, *13*, 23647–23654.

92 (22) Borah, B.; Zhang, H.; Snurr, R. Q. Diffusion of methane and
93 other alkanes in metal–organic frameworks for natural gas
94 storage. *Chem. Eng. Sci.* **2015**, *124*, 135–143.

95 (23) Nazarian, D.; Camp, J. S.; Sholl, D. S. A Comprehensive Set of
96 High-Quality Point Charges for Simulations of Metal–Organic
97 Frameworks. *Chem. Mater.* **2016**, *28*, 785–793.

98 (24) Rosen, A. S.; Iyer, S. M.; Ray, D.; Yao, Z.; Aspuru-Guzik, A.;
99 Gagliardi, L.; Notestein, J. M.; Snurr, R. Q. Machine learning the
100 quantum-chemical properties of metal–organic frameworks for
101 accelerated materials discovery. *Matter* **2021**.

102 (25) Chung, Y. G.; Bai, P.; Haranczyk, M.; Leperi, K. T.; Li, P.;
103 Zhang, H.; Wang, T. C.; Duerinck, T.; You, F.; Hupp, J. T.; et al.
104 Computational screening of nanoporous materials for hexane and
105 heptane isomer separation. *Chem. Mater.* **2017**, *29*, 6315–6328.

106 Boyd, P. G.; Chidambaram, A.; García-Díez, E.; Ireland, C. P.;
107 Daff, T. D.; Bounds, R.; Gladysiak, A.; Schouwink, P.; Moosavi,
108 S. M.; Maroto-Valer, M. M.; et al. Data-driven design of metal–
109 organic frameworks for wet flue gas CO₂ capture. *Nature* **2019**,
110 *576*, 253–256.

111 (26) Bai, P.; Jeon, M. Y.; Ren, L.; Knight, C.; Deem, M. W.;
112 Tsapatsis, M.; Siepmann, J. I. Discovery of optimal zeolites for
113 challenging separations and chemical transformations using
114 predictive materials modeling. *Nat. Commun.* **2015**, *6*, 5912.

115 Curtarolo, S.; Hart, G. L. W.; Nardelli, M. B.; Mingo, N.;
116 Sanvito, S.; Levy, O. The high-throughput highway to
117 computational materials design. *Nat. Mater.* **2013**, *12*, 191–201.

118 (27) Chung, Y. G.; Gómez-Gualdrón, D. A.; Li, P.; Leperi, K. T.;
119 Deria, P.; Zhang, H.; Vermeulen, N. A.; Stoddart, J. F.; You, F.;
120 Hupp, J. T.; et al. In silico discovery of metal–organic
121 frameworks for precombustion CO₂ capture using a genetic
122 algorithm. *Sci. Adv.* **2016**, *2*, e1600909.

123 <https://proceedings.mlr.press/v133/turner21a/turner21a.pdf>
124 <https://proceedings.mlr.press/v133/turner21a/turner21a.pdf>
125 (accessed Mar 13, 2024).

126 (28) Hern, J.; AlanAspuru-Guzik, E.-L. Parallel and Distributed
127 Thompson Sampling for Large-scale Accelerated Exploration of
128 Chemical Space.

129 (29) Shields, B. J.; Stevens, J.; Li, J.; Parasram, M.; Damani, F.;
130 Alvarado, J. I. M.; Janey, J. M.; Adams, R. P.; Doyle, A. G.
131 Bayesian reaction optimization as a tool for chemical synthesis.
132 *Nature* **2021**, *590*, 89–96.

133 Fang, L.; Makkonen, E.; Todorović, M.; Rinke, P.; Chen, X.
134 Efficient Amino Acid Conformer Search with Bayesian
135 Optimization. *J. Chem. Theory Comput.* **2021**, *17*, 1955–1966.

136 (30) 137
138

1 (34) Graff, D. E.; Shakhnovich, E. I.; Coley, C. W. Accelerating high-
2 throughput virtual screening through molecular pool-based active
3 learning. *Chem. Sci.* **2021**, *12*, 7866–7881.

4 (35) Gao, W.; Coley, C. W. The synthesizability of molecules
5 proposed by generative models. *J. Chem. Inf. Model.* **2020**, *60*,
6 5714–5723.

7 (36) Griffiths, R.-R.; Hernández-Lobato, J. M. Constrained Bayesian
8 optimization for automatic chemical design using variational
9 autoencoders. *Chem. Sci.* **2020**, *11*, 577–586.

10 (37) Gantzler, N.; Deshwal, A.; Doppa, J. R.; Simon, C. M. Multi-
11 fidelity Bayesian optimization of covalent organic frameworks
12 for xenon/krypton separations. *Digital Discovery* **2023**, *2*, 1937–
13 1956.

14 (38) Wang, M.; Kong, W.; Marten, R.; He, X.-C.; Chen, D.; Pfeifer,
15 J.; Heitto, A.; Kontkanen, J.; Dada, L.; Kürten, A.; et al. Rapid
16 growth of new atmospheric particles by nitric acid and ammonia
17 condensation. *Nature* **2020**, *581*, 184–189.

18 (39) Friedman, D.; Dieng, A. B. The Vendi Score: A Diversity
19 Evaluation Metric for Machine Learning. *arXiv* **2022**.

20 (40) Lim, J.; Fernández, C. A.; Lee, S. W.; Hatzell, M. C. Ammonia
21 and nitric acid demands for fertilizer use in 2050. *ACS Energy*
22 *Lett.* **2021**, *6*, 3676–3685.

23 (41) Hasan, M. H.; Mahlia, T. M. I.; Mofijur, M.; Rizwanul Fattah, I.
24 M.; Handayani, F.; Ong, H. C.; Silitonga, A. S. A comprehensive
25 review on the recent development of ammonia as a renewable
26 energy carrier. *Energies* **2021**, *14*, 3732.

27 (42) Smith, C.; Hill, A. K.; Torrente-Murciano, L. Current and future
28 role of Haber–Bosch ammonia in a carbon-free energy
29 landscape. *Energy Environ. Sci.* **2020**, *13*, 331–344.

30 (43) Kanjilal, B.; Masoumi, A.; Sharifi, N.; Noshadi, I. Ammonia
31 harms and diseases: ammonia corrosion hazards on human body
32 systems (liver, muscles, kidney, brain). In *Progresses in*
33 *ammonia: science, technology and membranes*; Elsevier, 2024;
34 pp. 307–324.

35 (44) Giddey, S.; Badwal, S. P. S.; Munnings, C.; Dolan, M. Ammonia
36 as a renewable energy transportation media. *ACS Sustain. Chem.*
37 *Eng.* **2017**, *5*, 10231–10239.

38 (45) Al-Breiki, M.; Bicer, Y. Technical assessment of liquefied natural
39 gas, ammonia and methanol for overseas energy transport based
40 on energy and exergy analyses. *Int. J. Hydrogen Energy* **2020**,
41 *45*, 34927–34937.

42 (46) Herrera, L. F.; Do, D. D.; Birkett, G. R. Comparative simulation
43 study of nitrogen and ammonia adsorption on graphitized and
44 nongraphitized carbon blacks. *J. Colloid Interface Sci.* **2008**,
45 *320*, 415–422.

46 (47) Moribe, S.; Chen, Z.; Alayoglu, S.; Syed, Z. H.; Islamoglu, T.;
47 Farha, O. K. Ammonia Capture within Isoreticular Metal–
48 Organic Frameworks with Rod Secondary Building Units. *ACS*
49 *Materials Lett.* **2019**, *1*, 476–480.

50 (48) Guo, L.; Hurd, J.; He, M.; Lu, W.; Li, J.; Crawshaw, D.; Fan, M.;
51 Sapchenko, S.; Chen, Y.; Zeng, X.; et al. Efficient capture and
52 storage of ammonia in robust aluminium-based metal–organic
53 frameworks. *Commun. Chem.* **2023**, *6*, 55.

54 (49) Kim, D. W.; Kang, D. W.; Kang, M.; Lee, J.-H.; Choe, J. H.;
55 Chae, Y. S.; Choi, D. S.; Yun, H.; Hong, C. S. High Ammonia
56 Uptake of a Metal–Organic Framework Adsorbent in a Wide
57 Pressure Range. *Angew. Chem. Int. Ed* **2020**, *59*, 22531–22536.

58 (50) Kim, D. W.; Kang, D. W.; Kang, M.; Choi, D. S.; Yun, H.; Kim,
59 S. Y.; Lee, S. M.; Lee, J.-H.; Hong, C. S. High Gravimetric and
60 Volumetric Ammonia Capacities in Robust Metal–Organic
61 Frameworks Prepared via Double Postsynthetic Modification. *J.*
62 *Am. Chem. Soc.* **2022**, *144*, 9672–9683.

63 (51) Shi, Y.; Wang, Z.; Li, Z.; Wang, H.; Xiong, D.; Qiu, J.; Tian, X.;
64 Feng, G.; Wang, J. Anchoring LiCl in the Nanopores of Metal–
65 Organic Frameworks for Ultra-High Uptake and Selective
66 Separation of Ammonia. *Angew. Chem. Int. Ed* **2022**, *61*,
67 e202212032.

68 (52) Han, X.; Lu, W.; Chen, Y.; da Silva, I.; Li, J.; Lin, L.; Li, W.;
69 Sheveleva, A. M.; Godfrey, H. G. W.; Lu, Z.; et al. High
70 Ammonia Adsorption in MFM-300 Materials: Dynamics and
71 Charge Transfer in Host–Guest Binding. *J. Am. Chem. Soc.* **2021**,
72 *143*, 3153–3161.

73 (53) Luo, L.; Liu, Y.; Wu, Z.; Liu, J.; Cao, X.; Lin, J.; Ling, R.; Luo,
74 X.; Wang, C. Macromolecular–metal complexes induced by
75 Co(II) with polymer and flexible ligands for ammonia uptake
76 compared with MOFs. *Chemical Engineering Journal* **2022**, *448*,
77 137626.

78 (54) Moosavi, S. M.; Nandy, A.; Jablonka, K. M.; Ongari, D.; Janet, J.
79 P.; Boyd, P. G.; Lee, Y.; Smit, B.; Kulik, H. J. Understanding the
80 diversity of the metal–organic framework ecosystem. *Nat.*
81 *Commun.* **2020**, *11*, 4068.

82 (55) Willems, T. F.; Rycroft, C. H.; Kazi, M.; Meza, J. C.; Haranczyk,
83 M. Algorithms and tools for high-throughput geometry-based
84 analysis of crystalline porous materials. *Micropor. Mesopor.*
85 *Mat.* **2012**, *149*, 134–141.

86 (56) Wei, Q.; Lucero, J. M.; Crawford, J. M.; Way, J. D.; Wolden, C.
87 A.; Carreon, M. A. Ammonia separation from N2 and H2 over
88 LTA zeolitic imidazolate framework membranes. *J. Memb. Sci.*
89 **2021**, *623*, 119078.

90 (57) Dubbeldam, D.; Calero, S.; Ellis, D. E.; Snurr, R. Q. RASPA:
91 molecular simulation software for adsorption and diffusion in
92 flexible nanoporous materials. *Mol. Simul.* **2016**, *42*, 81–101.

93 (58) Dubbeldam, D.; Torres-Knoop, A.; Walton, K. S. On the inner
94 workings of Monte Carlo codes. *Mol. Simul.* **2013**, *39*, 1253–
95 1292.

96 (59) Widom, B. Some topics in the theory of fluids. *J. Chem. Phys.*
97 **1963**, *39*, 2808–2812.

98 (60) Finfinite crystals, accurate and efficient calcu-.

99 (61) Karasawa, N.; Goddard, W. A. Acceleration of convergence for
100 lattice sums. *J. Phys. Chem.* **1989**, *93*, 7320–7327.

101 (62) Chen, B.; Siepmann, J. I. Transferable Potentials for Phase
102 Equilibria. 3. Explicit-Hydrogen Description of Normal Alkanes.
103 *J. Phys. Chem. B* **1999**, *103*, 5370–5379.

104 (63) Zhang, L.; Siepmann, J. I. Development of the trappe force field
105 for ammonia. *Collect. Czechoslov. Chem. Commun.* **2010**, *75*,
106 577–591.

107 (64) Jorgensen, W. L.; Chandrasekhar, J.; Madura, J. D.; Impey, R.
108 W.; Klein, M. L. Comparison of simple potential functions for
109 simulating liquid water. *J. Chem. Phys.* **1983**, *79*, 926.

110 (65) González, M. A.; Abascal, J. L. F. The shear viscosity of rigid
111 water models. *J. Chem. Phys.* **2010**, *132*, 096101.

112 (66) Aragones, J. L.; Vega, C. Plastic crystal phases of simple water
113 models. *J. Chem. Phys.* **2009**, *130*, 244504.

114 (67) Guillot, B.; Guissani, Y. Quantum effects in simulated water by
115 the Feynman–Hibbs approach. *J. Chem. Phys.* **1998**, *108*, 10162–
116 10174.

117 (68) Sesé, L. M. Study of the Feynman–Hibbs effective potential
118 against the path-integral formalism for Monte Carlo simulations
119 of quantum many-body Lennard–Jones systems. *Mol. Phys.*
120 **1994**, *81*, 1297–1312.

121 (69) Mayo, S. L.; Olafson, B. D.; Goddard, W. A. DREIDING: a
122 generic force field for molecular simulations. *J. Phys. Chem.*
123 **1990**, *94*, 8897–8909.

124 (70) Rappe, A. K.; Casewit, C. J.; Colwell, K. S.; Goddard, W. A.;
125 Skiff, W. M. UFF, a full periodic table force field for molecular
126 mechanics and molecular dynamics simulations. *J. Am. Chem.*
127 *Soc.* **1992**, *114*, 10024–10035.

128 (71) Moghadam, P. Z.; Ghosh, P.; Snurr, R. Q. Understanding the
129 effects of preadsorbed perfluoroalkanes on the adsorption of
130 water and ammonia in mofs. *J. Phys. Chem. C* **2015**, *119*, 3163–
131 3170.

132 (72) Oliveira, F. L.; Cleeton, C.; Neumann Barros Ferreira, R.; Luan,
133 B.; Farmahini, A. H.; Sarkisov, L.; Steiner, M. CRAFTED: An
134 exploratory database of simulated adsorption isotherms of metal–
135 organic frameworks. *Sci. Data* **2023**, *10*, 230.

136 (73) Ghosh, P.; Kim, K. C.; Snurr, R. Q. Modeling water and
137 ammonia adsorption in hydrophobic metal–organic frameworks:
138 single components and mixtures. *J. Phys. Chem. C* **2014**, *118*,
139 1102–1110.

1 (74) Dokur, D.; Keskin, S. Effects of force field selection on the
2 computational ranking of mofs for CO₂ separations. *Ind. Eng.*
3 *Chem. Res.* **2018**, *57*, 2298–2309.

4 (75) Anderson, R.; Biong, A.; Gómez-Gualdrón, D. A. Adsorption
5 isotherm predictions for multiple molecules in MOFs using the
6 same deep learning model. *J. Chem. Theory Comput.* **2020**.

7 (76) Argueta, E.; Shaji, J.; Gopalan, A.; Liao, P.; Snurr, R. Q.;
8 Gómez-Gualdrón, D. A. Molecular Building Block-Based
9 Electronic Charges for High-Throughput Screening of Metal-
10 Organic Frameworks for Adsorption Applications. *J. Chem.*
11 *Theory Comput.* **2018**, *14*, 365–376.

12 (77) Kancharlapalli, S.; Gopalan, A.; Haranczyk, M.; Snurr, R. Q. Fast
13 and Accurate Machine Learning Strategy for Calculating Partial
14 Atomic Charges in Metal–Organic Frameworks. *J. Chem. Theory*
15 *Comput.* **2021**, *17*, 3052–3064.

16 (78) Liu, S.; Luan, B. Benchmarking various types of partial atomic
17 charges for classical all-atom simulations of metal-organic
18 frameworks. *Nanoscale* **2022**, *14*, 9466–9473.

19 (79) Aziz, M.; Wijayanta, A. T.; Nandiyanto, A. B. D. Ammonia as
20 effective hydrogen storage: A review on production, storage and
21 utilization. *Energies* **2020**, *13*, 3062.

22 (80) Wang, Q.; Guo, J.; Chen, P. Recent progress towards mild-
23 condition ammonia synthesis. *Journal of Energy Chemistry*
24 **2019**, *36*, 25–36.

25 (81) Han, G.-F.; Li, F.; Chen, Z.-W.; Coppex, C.; Kim, S.-J.; Noh, H.-
26 J.; Fu, Z.; Lu, Y.; Singh, C. V.; Siahrostami, S.; et al.
27 Mechanochemistry for ammonia synthesis under mild
28 conditions. *Nat. Nanotechnol.* **2021**, *16*, 325–330.

29 (82) Guan, Y.; Wen, H.; Cui, K.; Wang, Q.; Gao, W.; Cai, Y.; Cheng,
30 Z.; Pei, Q.; Li, Z.; Cao, H.; et al. Light-driven ammonia synthesis
31 under mild conditions using lithium hydride. *Nat. Chem.* **2024**.

32 (83) van 't Veer, K.; Engelmann, Y.; Reniers, F.; Bogaerts, A. Plasma-
33 Catalytic Ammonia Synthesis in a DBD Plasma: Role of
34 Microdischarges and Their Afterglows. *J. Phys. Chem. C* **2020**,
35 *124*, 22871–22883.

36 (84) Wang, Y.; Yang, W.; Xu, S.; Zhao, S.; Chen, G.; Weidenkaff, A.;
37 Hardacre, C.; Fan, X.; Huang, J.; Tu, X. Shielding Protection by
38 Mesoporous Catalysts for Improving Plasma-Catalytic Ambient
39 Ammonia Synthesis. *J. Am. Chem. Soc.* **2022**, *144*, 12020–
40 12031.

41 (85) Namboothiri, N. V.; Soman, A. R. Consequence assessment of
42 anhydrous ammonia release using CFD-probit analysis. *Proc.*
43 *Safety Prog.* **2018**, *37*, 525–534.

44 (86) Moghadam, P. Z.; Fairén-Jimenez, D.; Snurr, R. Q. Efficient
45 identification of hydrophobic MOFs: application in the capture
46 of toxic industrial chemicals. *J. Mater. Chem. A* **2016**, *4*, 529–
47 536.

48 (87) Zhang, H.; Snurr, R. Q. Computational Study of Water
49 Adsorption in the Hydrophobic Metal–Organic Framework ZIF-
50 8: Adsorption Mechanism and Acceleration of the Simulations.
51 *J. Phys. Chem. C* **2017**, *121*, 24000–24010.

52 (88) Rasmussen, C. E.; Williams, C. K. I. *Gaussian processes for*
53 *machine learning*; The MIT Press, 2005.

54 (89) Rogers, D.; Hahn, M. Extended-connectivity fingerprints. *J.*
55 *Chem. Inf. Model.* **2010**, *50*, 742–754.

56 (90) Weininger, D. SMILES, a chemical language and information
57 system. 1. Introduction to methodology and encoding rules. *J.*
58 *Chem. Inf. Model.* **1988**, *28*, 31–36.

59 (91) Willett, P.; Barnard, J. M.; Downs, G. M. Chemical Similarity
60 Searching. *J. Chem. Inf. Comput. Sci.* **1998**, *38*, 983–996.

61 (92) Mukadum, F.; Nguyen, Q.; Adrián, D. M.; Appleby, G.; Chen,
62 R.; Dang, H.; Chang, R.; Garnett, R.; Lopez, S. A. Efficient
63 Discovery of Visible Light-Activated Azoarene Photoswitches
64 with Long Half-Lives Using Active Search. *J. Chem. Inf. Model.*
65 **2021**, *61*, 5524–5534.

66 (93) Gantzler, N.; Deshwal, A.; Doppa, J. R.; Simon, C. Multi-fidelity
67 Bayesian Optimization of Covalent Organic Frameworks for
68 Xenon/Krypton Separations. **2023**.

69 (94) Lin, J. Divergence measures based on the Shannon entropy. *IEEE*
70 *Trans. Inform. Theory* **1991**, *37*, 145–151.

71 (95) pauerigi.tu-graz.ac.at, P. Using Confidence Bounds for
72 Exploitation-Exploration Trade-offs.

73 (96) Taw, E.; Neaton, J. B. Accelerated discovery of ch₄ uptake
74 capacity metal–organic frameworks using bayesian optimization.
75 *Adv. Theory Simul.* **2022**, *5*.

76 (97) Cox, M. A. A.; Cox, T. F. Multidimensional Scaling. In
77 *Handbook of data visualization*; Springer Berlin Heidelberg:
78 Berlin, Heidelberg, 2008; pp. 315–347.

79 (98) Tian, X.; Qiu, J.; Wang, Z.; Chen, Y.; Li, Z.; Wang, H.; Zhao, Y.;
80 Wang, J. A record ammonia adsorption by calcium chloride
81 confined in covalent organic frameworks. *Chem. Commun.* **2022**,
82 58, 1151–1154.

83 (99) Freitas, R.; Asta, M.; de Koning, M. Nonequilibrium free-energy
84 calculation of solids using LAMMPS. *Comp. Mater. Sci.* **2016**,
85 *112*, 333–341.

86 (100) Anderson, R.; Gómez-Gualdrón, D. A. Large-Scale Free Energy
87 Calculations on a Computational Metal–Organic Frameworks
88 Database: Toward Synthetic Likelihood Predictions. *Chem.*
89 *Mater.* **2020**, *32*, 8106–8119.

90 (101) Nandy, A.; Duan, C.; Kulik, H. J. Using Machine Learning and
91 Data Mining to Leverage Community Knowledge for the
92 Engineering of Stable Metal–Organic Frameworks. *J. Am. Chem.*
93 *Soc.* **2021**, *143*, 17535–17547.

94 (102) Nandy, A.; Terrones, G.; Arunachalam, N.; Duan, C.; Kastner,
95 D. W.; Kulik, H. J. MOFSimplify, machine learning models with
96 extracted stability data of three thousand metal-organic
97 frameworks. *Sci. Data* **2022**, *9*, 74.

98 (103) Zou, Y.; Li, L.; Li, Y.; Chen, S.; Xie, X.; Jin, X.; Wang, X.; Ma,
99 C.; Fan, G.; Wang, W. Restoring Cardiac Functions after
100 Myocardial Infarction-Ischemia/Reperfusion via an Exosome
101 Anchoring Conductive Hydrogel. *ACS Appl. Mater. Interfaces*
102 **2021**, *13*, 56892–56908.

103 (104) Kloutse, F. A.; Zacharia, R.; Cossement, D.; Chahine, R.
104 Specific heat capacities of MOF-5, Cu-BTC, Fe-BTC, MOF-177
105 and MIL-53 (Al) over wide temperature ranges: Measurements
106 and application of empirical group contribution method.
107 *Micropor. Mesopor. Mat.* **2015**, *217*, 1–5.

108 (105) Cardoso, J. S.; Silva, V.; Rocha, R. C.; Hall, M. J.; Costa, M.;
109 Eusébio, D. Ammonia as an energy vector: Current and future
110 prospects for low-carbon fuel applications in internal combustion
111 engines. *J. Clean. Prod.* **2021**, *296*, 126562.

112 (106) Erdemir, D.; Dincer, I. A perspective on the use of ammonia as a
113 clean fuel: Challenges and solutions. *Int. J. Energy Res.* **2021**, *45*,
114 4827–4834.

115

116 TOC

